A Simulation of a Squall Line Using a Nonhydrostatic Cloud Model with a 5-km Horizontal Grid

RICHARD S. HEMLER, FRANK B. LIPPS,* AND BRUCE B. ROSS

Geophysical Fluid Dynamics Laboratory/NOAA, Princeton University, Princeton, New Jersey

(Manuscript received 3 April 1990, in final form 12 April 1991)

ABSTRACT

A three-dimensional nonhydrostatic cloud model is used to simulate the squall line observed in central Texas on 11 April 1979. The cloud model covers an area 400 × 400 km^2 with a 5-km horizontal resolution and is supplied initial and boundary conditions by a larger hydrostatic mesoscale model.

The model produces a back-building squall line ahead of the surface cold front, as would be expected based on an analysis of the pre-squall-line environment. A well-defined gust front and cold pool develop with the squall line. At the end of the 5-h simulation, deep convection is found along a line nearly 400 km long. The simulated squall line compares favorably both with observations and with a higher-resolution model simulation in an environment of similar shear, suggesting that the 5-km horizontal resolution is adequately representing the significant features of the squall line.

The major shortcoming of this study is the failure of the cloud model to produce the observed squall line at the proper time. Without the observed small-scale forcing, which was unresolved in the Severe Environmental Storms and Mesoscale Experiment (SESAME) dataset, the model is unable to generate the squall line until a larger-scale convergence area evolves, some 2–3 h after the appearance of the observed squall line.

1. Introduction

A number of three-dimensional numerical studies of squall lines and the convection associated with them have been published in recent years. One of two approaches has generally been taken. Either a nonhydrostatic cloud model with horizontal grid length of 2 km or less was used to simulate the convection in only a portion of the squall line (e.g., Weisman and Klemp 1982; Weisman et al. 1988; Redelsberger and Lafore 1988), or a hydrostatic mesoscale model with horizontal grid length greater than 10 km was employed to simulate the mesoscale features of the line and its environment, without resolving the smaller-scale convection (e.g., Chang et al. 1981; Zhang and Fritsch 1986; Ross, 1987).

A third approach is to develop a nested mesoscale–cloud-scale model, providing high resolution in areas of strong convection while covering a sufficient area with the mesoscale model to enclose the squall-line circulation and provide accurate boundary forcing for the cloud model. Most previously reported nested-grid models used in convection and mesoscale studies have used the same dynamical model in all the nests, changing only the resolution and resolution-dependent parameters between the nests (e.g., Kurihara et al. 1979; Blechman 1981; Zack et al. 1983; Klemp and Rotunno 1983; Clark and Farley 1984). The model proposed here uses a different approach in which a hydrostatic mesoscale model is utilized for the outer nest, and a nonhydrostatic cloud model for the inner nest. This approach has also been used in the United Kingdom Meteorological Office model (Bell 1987).

This study presents the results of the first step in the development of such a model. Here we determine whether the use of 5-km horizontal resolution in the cloud model is adequate to represent the important features of a squall line. Such a large grid increment is needed so that the model can cover sufficient area without being overly expensive, although ultimately a 2–3-km grid may be employed.

The squall line selected for this study occurred in north-central Texas during the first observing day of the Severe Environmental Storms and Mesoscale Experiment (SESAME), 10–11 April 1979. A discussion of the synoptic and mesoscale setting and the squall line itself is contained in section 2. Because of the severity of the convection and the availability of higher-than-normal-resolution data from SESAME, several mesoscale numerical simulations have been performed for this case (e.g., Kuo and Anthes 1984; Kalb 1985; Ross 1987). In the model study of Ross (1987), a southwest–northeast line of precipitation was produced

* Dr. Frank B. Lipps died on 9 November 1990. This is one of several papers upon which he was working at the time of his death.

Corresponding author address: Mr. Richard S. Hemler, NOAA/GFDL, Princeton University, Princeton, NJ 08542.

in the vicinity of the observed squall line. Associated with this precipitation was large-scale low-level convergence, a forcing that would be expected to produce a squall line in the cloud model. Thus, this case was chosen for the present study.

The study is organized as follows. First, the mesoscale model is integrated over a domain of 1000×1000 km^2 using a horizontal resolution of 20 km. Data from this integration are then used to initialize a 400×400^2 cloud model located in the region of the squall line. The cloud model is integrated forward in time, using lateral boundary forcing obtained from the mesoscale-model integration. The model is described in section 3.

The remainder of the paper discusses the results of the numerical integration. In section 4, the initial conditions of the cloud model are assessed through comparison with observational data. The model results are presented in section 5 and compared with observations and results of both a lower-resolution simulation with the current model and a previous higher-resolution study made in an environment of similar shear. A review and discussion of the results is given in section 6.

2. The observed squall line

As stated in Ross (1987), the synoptic-scale conditions of 10–11 April 1979 have been described by several authors (Moore and Fuelberg 1981). Ross (1987) gives a concise description of the mesoscale features of the squall line. This section briefly reviews the synoptic and mesoscale environmental conditions and describes the evolution of the squall line and associated severe weather.

Synoptic charts at 1200 UTC 10 April 1979 (not shown here, see Moore and Fuelberg 1981) featured a surface low on the Colorado–Wyoming border with a cold front trailing southward through western New Mexico. This surface low was associated with an upper-level trough that extended southward through central Washington into New Mexico. High pressure was north of the Great Lakes, and a stationary front lay along the Gulf Coast.

Between 1200 UTC 10 April and 0000 UTC 11 April, the trough dug southeastward, resulting in a slight deepening of the surface low and its movement into central Colorado. The approaching upper-level trough also induced a surface-pressure trough in west Texas, which was detectable in mesoscale surface analyses as early as 1500 UTC (Moller 1980). By 1700 UTC, a mesolow had developed in the pressure trough, and a dry line had begun to form, marking the intersection of the warm, moist south-to-southeast winds blowing off the Gulf of Mexico with the hot, dry south–southwest winds blowing off the Mexican plateau. The stationary front along the Gulf Coast began moving north as a warm front, reaching the Oklahoma–Texas border by 0000 UTC 11 April (Fig. 1). Southwesterly winds at 700 hPa brought warm, dry air over the moist, low-level gulf air behind this front. Convective instability increased during this period, as indicated by the lifted-index analyses in Moore and Fuelberg (1981). Finally,

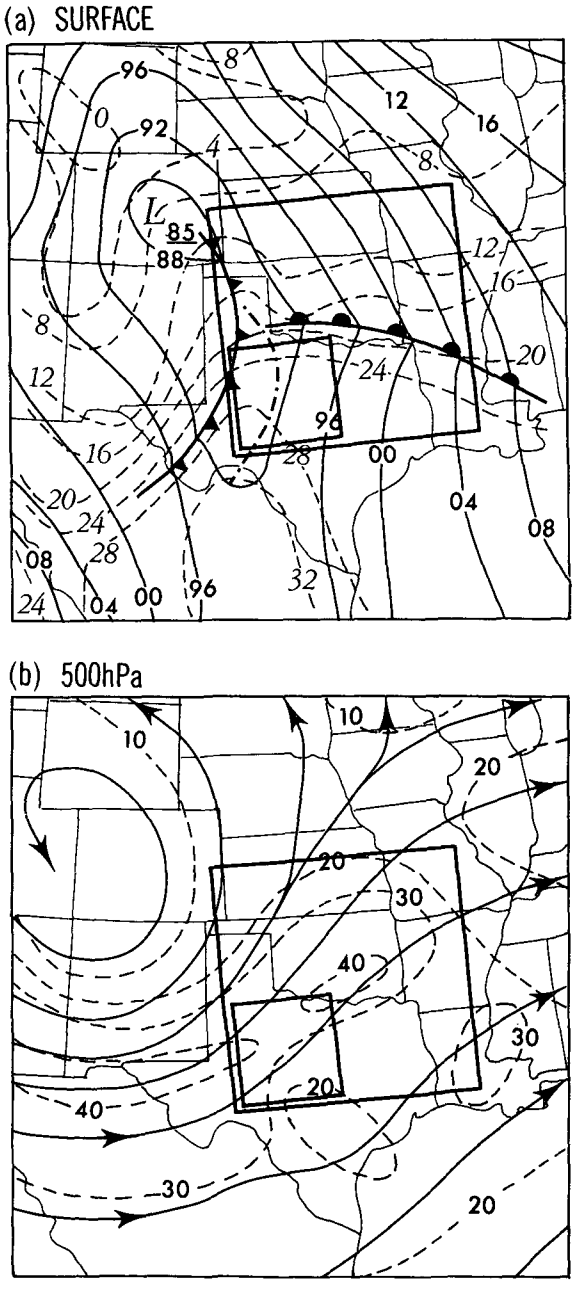

FIG. 1. Synoptic charts at 0000 UTC 11 April 1979. (a) Surface conditions, including sea level pressure [solid contours, in units of hectopascals (hPa) with only the last two digits shown] and surface isotherms [dashed contours in units of degrees Celsius (°C)]. Dry line is indicated by dash–dot line. (b) 500-hPa flow field [dashed contours indicate isotachs, in units of meters per second (m s^{-1})]. Large and small boxes denote boundaries of mesoscale and cloud-model domains, respectively. Figure adapted from Figs. 17 and 18 of Anthes et al. (1982); also shown in Ross (1987).

a jet streak had moved around the base of the upper trough and began to enter west-central Texas. Surface and 500-hPa synoptic maps at 0000 UTC 11 April 1979 are shown in Fig. 1.

With so many favorable conditions present, convection quickly developed, and by 1900 UTC 10 April an area of thunderstorms was observed in the southern part of the Texas Panhandle. Over the next few hours, this convection and its associated mesolow moved northeastward to the Oklahoma border producing tornadoes and severe thunderstorms, including the Wichita Falls tornado.

The squall line of this study evolved from the narrow northeast–southwest line of clouds visible in the 2300 UTC 10 April satellite picture (Fig. 2a). The line grew slowly during the next 2 h (Fig. 2b), but more rapid development began after 0100 UTC in response to a developing mesolow north of San Angelo, Texas (SJT) (Fig. 3a). Surface pressures fell 1–2 mb between 0100 and 0200 UTC, and the flow became southeasterly drawing moist, gulf air westward into the cloud line and raising the dewpoint at Abilene, Texas (ABI) by 9 K during the hour. Precipitation from the line was first detected on radar at 0135 UTC.

Figure 3 is a composite of radar echoes, satellite cloud images, and severe weather reports (reports taken from Alberty et al. 1979) between 0200 and 0600 UTC showing the location of the significant weather along with its time of occurrence. After several tornadoes were reported northeast of SJT between 0315 and 0400 UTC, there was a lull in severe weather reports between 0400 and 0515 UTC. However, in the following hour, severe weather was reported in two areas, one near Mineral Wells (MWL) and the other to the south and

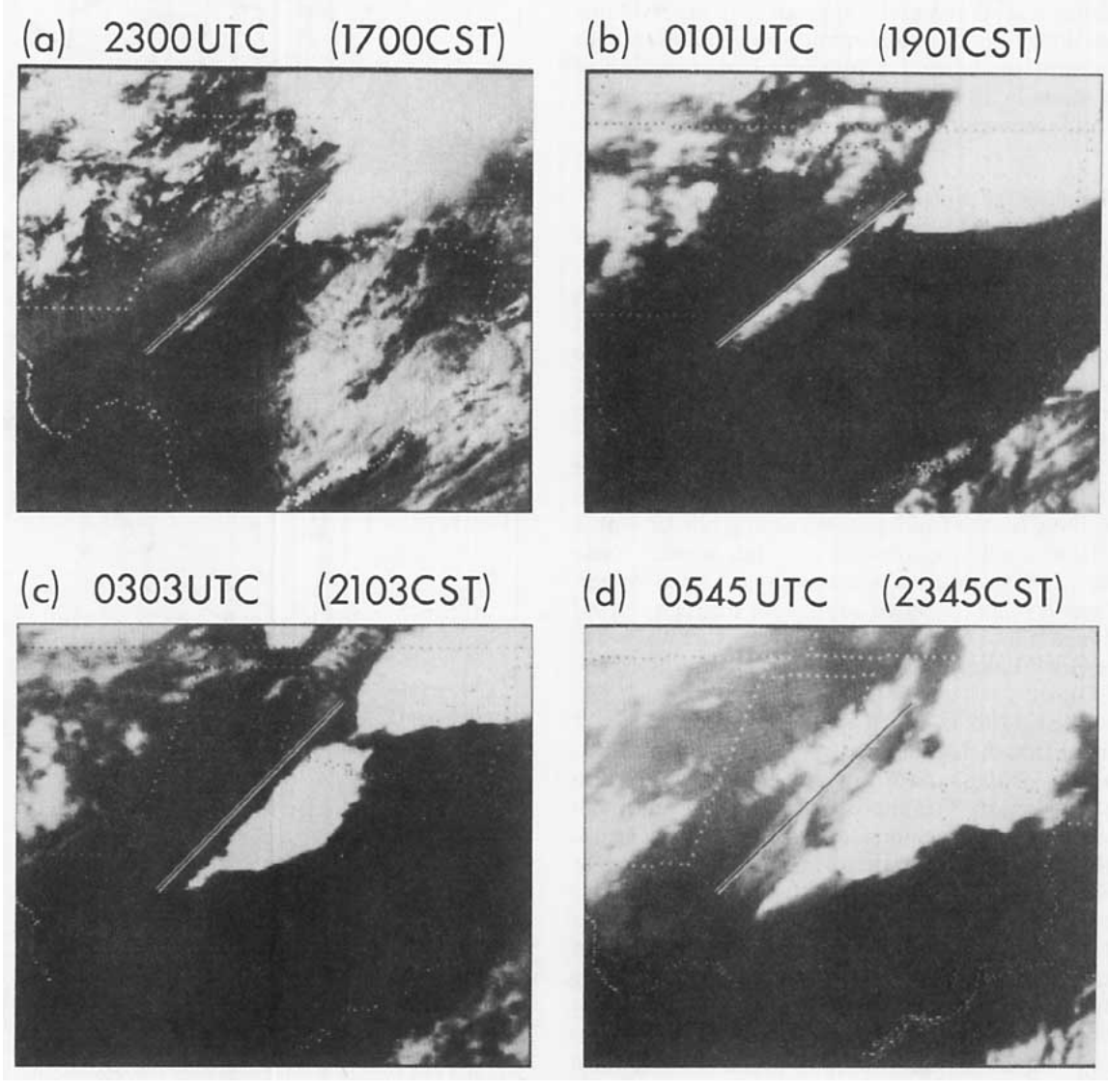

FIG. 2. Satellite photographs showing (a) visible and (b)–(d) infrared imagery. A reference line has been added at the same location in each frame to indicate the position of the initial development of the cloud system. Figure taken from Ross (1987).

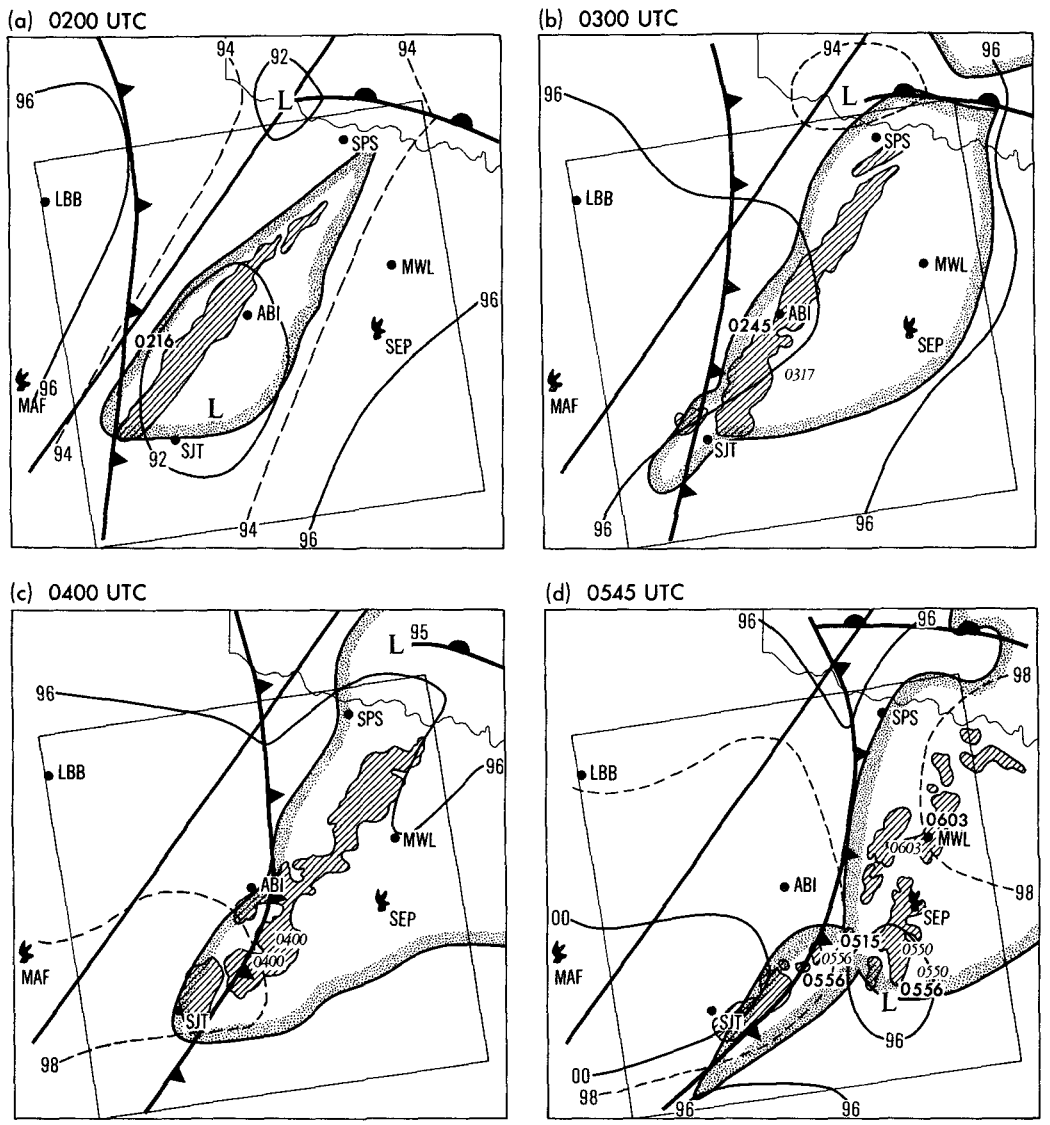

FIG. 3. Composite of radar, satellite, and surface observations at 0200, 0300, 0400, and 0545 UTC 11 April 1979. Indicated are the radar sites at Midland (MAF) and Stephenville (SEP) and surface stations at Lubbock (LBB), Wichita Falls (SPS), Mineral Wells (MWL), San Angelo (SJT), and Abilene (ABI). The box denotes the boundaries of the cloud-model domain. Hatched areas represent radar echoes; the solid line and adjoining stippling indicate the satellite-observed cloud extent. Times indicate location of occurrences of tornadoes (italics) and hail or high wind (roman font). Solid line is the reference line of Fig. 2. Contours are isobars (hPa, with only the last two digits shown). Frontal positions obtained from surface mesoanalyses.

southwest of Stephenville (SEP). Severe weather ended by 0630 UTC, as the remaining cells continued eastward and slowly dissipated.

3. The cloud model

a. The model formulation

The cloud model (subsequently to be referred to as the CLM) is described in Lipps and Hemler (1982), Lipps and Hemler (1986), and Lipps and Hemler (1988), hereafter referred to as LH82, LH86, and LH88, respectively. A brief review of the basic model will be presented here, with emphasis placed on model features not described in previous papers.

1) MODEL EQUATIONS

The model uses the deep anelastic approximation in which base-state density ρ_0 is a function of height only. Prognostic equations are solved for the momentum components u, v, and w, the potential temperature θ, the water vapor mixing ratio q_v, the cloud-water

mixing ratio q_c, and the rainwater mixing ratio q_r. The pressure ϕ is obtained diagnostically from the solution of a Poisson equation. The momentum equations contain the standard advection, subgrid-scale mixing, buoyancy, and pressure gradient terms of LH86, but in addition contain the vertical Coriolis terms and a Newtonian damping (sponge) in upper levels to reduce the amplitude of gravity waves reflected from the upper boundary. The equations are solved using centered time and space differences and include a Robert (1966) filter and a fourth-order horizontal diffusion term, as described in LH86. Details on the formulation of the Newtonian smoother are contained in appendix A.

The θ and q_v equations are also solved using centered time and space differences and a Robert filter. They contain advection, subgrid-scale mixing, condensation, and evaporation terms, as well as fourth-order horizontal diffusion terms and a Newtonian damping term in the θ equation at upper levels. Because q_v is integrated with a centered-difference scheme, spurious negative and positive values of q_v may be created through advection truncation errors. To compensate for these errors, an additional vertical eddy viscosity term has been added to the q_v equation. The eddy viscosity coefficient K_q for this term is given by

$$K_q = c^2\left(\frac{|\delta_z q_v|}{\bar{q}_v{}^z} - 1\right)^2, \qquad (1)$$

where $\delta_z q_v$ is the vertical difference of q_v, $\bar{q}_v{}^z$ is the vertical average, and c^2 is a constant set equal to 400 $m^2\ s^{-1}$. The term is applied only at points where 1) the vertical velocity is downward, and 2) the expression in brackets is ≥ 0, indicating that the vertical difference of q_v is large compared to its mean value. These conditions generally exist when negative values of q_v are being created. Tests have shown the term to be quite effective in reducing spurious q_v generation; however, it does not eliminate it entirely, particularly when strong downdrafts are present near cloud top in a very dry environment, as in the current study. Any negative values of q_v, not eliminated by this term, are set to zero.

The q_c and q_r equations are integrated with the Clark (1979) scheme, unchanged from the form used in LH86. The motivation for choosing this scheme is to eliminate the problem of numerically generated spurious negative values of q_c and q_r. The bulk cloud physics follows that of Kessler (1969) where the cloud-water q_c moves with the air and the rainwater q_r has the fall velocity $-V_T$ relative to the air. A detailed description of the present bulk cloud physics is given in appendix A.

The subgrid-scale formulation follows that described in LH88. An eddy viscosity is calculated based on both deformation and unstable stratification effects (Lilly 1962; Clark 1979). In regions of unstable stratification, mixing is isotropic with strong mixing in both the vertical and horizontal. In regions of stable stratification, the turbulence is transversely isotropic (Kirwan 1969; Williams 1972), with weaker mixing in the vertical than in the horizontal. Changes from the subgrid-scale formulation of LH88 are discussed in appendix A.

2) BOUNDARY CONDITIONS

Upper and lower boundary conditions remain as described in LH86, with the exception of a change to the drag-law formulation to make it more appropriate for use over land rather than over sea. The vertical momentum fluxes $\rho_0\overline{u'w'}$ and $\rho_0\overline{v'w'}$ at the surface are given by

$$\rho_0\overline{u'w'} = -\rho_0 C_D V_{100\ \mathrm{m}} u_{100\ \mathrm{m}} \qquad (2)$$

$$\rho_0\overline{v'w'} = -\rho_0 C_D V_{100\ \mathrm{m}} v_{100\ \mathrm{m}}, \qquad (3)$$

where $V_{100\ \mathrm{m}}$ is the horizontal wind speed at a height of 100 m, $u_{100\ \mathrm{m}}$ and $v_{100\ \mathrm{m}}$ are the u and v wind components at 100 m, and $C_D = 2 \times 10^{-3}$. The winds at 100 m are determined by a downward extrapolation of the wind gradient that exists between the first and second interior points in the model. Winds at 100 m are used rather than the value at the lowest grid point (243 m), since the basis of the drag-law formulation is the assumption of a constant stress layer, which often is shallower than 243 m. Vertical fluxes of θ and q_v at the surface are set to zero.

The CLM has open lateral boundaries that allow waves to propagate out of the domain with a minimum amount of reflection. Boundary conditions for normal velocities are given by the Sommerfeld radiation condition in a form similar to that presented by Orlanski (1976). Specification at inflow boundaries and extrapolation at outflow boundaries have been found to produce satisfactory results for the other prognostic variables (Klemp and Wilhelmson 1978; Clark 1979). A detailed discussion of the scheme for normal velocities is given in appendix B.

b. The mesoscale model

The mesoscale model (to be referred to subsequently as the MSM) used in this study to supply initial conditions and boundary forcing is that described in Ross (1987), but it has higher vertical resolution. It is an anelastic, hydrostatic model using Cartesian coordinates with height z as the vertical coordinate. The model contains prognostic equations for the horizontal wind components u and v, the potential temperature θ, the water vapor mixing ratio q_v, and cloud-water mixing ratio q_c. Cloud water condenses (evaporates) when the relative humidity becomes greater than (less than) 100%. Rainwater is produced when cloud-water density exceeds 1.5 $g\ m^{-3}$; it is not allowed to fall, but is removed immediately from the system and accumulated as precipitation.

A fourth-order diffusion scheme is used in the horizontal to control noise, while a Richardson-number–dependent mixing coefficient is used in the vertical (Ross and Orlanski 1982). At the surface, a bulk aerodynamic formulation is used to transfer momentum between the earth and the atmosphere. A prescribed surface temperature based on observations is used to provide effects of surface heating, while the water vapor flux across the surface is set to zero.

The horizontal domain extends 1000 km in both the east–west and north–south directions, with a grid resolution of $\Delta x = \Delta y = 20$ km, over the portion of the south-central United States shown in Fig. 1. Model top is 15 km above sea level, or 14.6 km above the model's lower boundary, which is set at 400 m above sea level. Ross (1987) justifies the use of a constant-height lower boundary for this study. A time step of 22.5 s is used in the mesoscale model.

A significant change from the model of Ross (1987) is the halving of the vertical grid interval to 486.7 m. This change provides increased vertical resolution and eliminates the need for vertical interpolation to produce initial and boundary data for the cloud model, which is normally used with a vertical resolution of 500 m in midlatitude convection studies.

The model has open lateral boundary conditions and uses the local normal velocity to determine whether inflow or outflow is present. Time-dependent boundary forcing to drive the MSM was obtained from data supplied by Dayton Vincent and Thomas Carney of Purdue University. The data were generated from the SESAME dataset, following the procedures described by Vincent et al. (1981) and Vincent and Carney (1982). Ross (1987) describes the technique used to prepare this dataset for use in the MSM. Further discussion of the MSM may be found in Ross (1987) and Ross and Orlanski (1982).

c. *Defining the CLM domain*

Figure 1 shows the locations of the MSM and CLM domains. It is necessary to position the CLM domain in the southwestern quadrant of the MSM domain to contain the squall line and its circulation. The CLM is cast in Cartesian coordinates with $\Delta x = \Delta y = 5$ km, and $\Delta z = 486.7$ m. The model has 80 grid points in both the x and y directions, giving a total horizontal domain size of 400×400 km^2. Model top is 17.52 km above the lower boundary, 2.9 km ($6\Delta z$) higher than that of the mesoscale model. This change was made so the model could accommodate the observed cloud tops of 53 000 ft (16.2 km). A time step of 10 s is used throughout the integration.

The MSM simulation was begun at 1200 UTC 10 April, well before the development of the Texas squall line. Integration of the CLM was begun 13 h later at 0100 UTC 11 April, just prior to the first radar detection of precipitation in the line and more than 2 h before deep convection developed in the MSM simulation. This allows the CLM to have the opportunity to better simulate the onset time of the deep convection. Experimentation with different starting times for the CLM simulation failed to produce any significantly different results.

d. *Initial conditions and boundary forcing*

Initial conditions and boundary forcing are supplied to the CLM from the MSM simulation rather than directly from the SESAME dataset. Initial conditions taken from the MSM after several hours of integration contain smaller-scale features than are present in the lower-resolution SESAME dataset, as will be seen in section 4. Such features as stronger horizontal temperature and moisture gradients, and more concentrated convergence areas are desirable in the initial fields, since they aid in the development of deep convection. Interpolated initial fields based solely on the SESAME dataset would not contain such small-scale features, and their absence would likely have an adverse effect on the simulation.

Boundary forcing is also taken from the MSM to be consistent with the initial conditions. It is likely that this forcing is similar to the forcing that would be obtained from the SESAME dataset, since the CLM inflow boundaries are so near the MSM boundaries. There would be little opportunity for the MSM to significantly modify this forcing within the distance of only a few grid points.

1) INITIAL DATA

Initial data for the CLM are obtained by interpolating the gridded data from the MSM simulation, using the 16-point interpolation scheme of Shapiro (1972) and following the principles presented in Ross and Orlanski (1982). Rather than interpolating u and v, vorticity and divergence fields are generated on the 20-km grid and then interpolated, resulting in smoother u and v fields than are obtained by direct interpolation. The vertical velocity field w is then obtained from the continuity equation.

Interpolation of θ is done straightforwardly using the Shapiro scheme. Relative humidity, rather than the mixing ratio, is interpolated to the 5-km grid, since the expression for saturation mixing ratio differs between the two models. By interpolating the relative humidity, the relative saturation deficit is maintained during the initialization. Cloud- and rainwater fields are initialized to zero in the CLM, since only a trivial amount of cloud water is present within the CLM domain at 0100 UTC, and this is located along the northern boundary.

The above steps provide initial data at model levels between the surface and the MSM top at 14.6 km. Initial data are also required for the six additional levels

between 14.6 and 17.5 km. Since this region is to be used primarily as a sponge, the initial conditions are made as simple as possible. The horizontal wind components at each point on these levels are set equal to the horizontal average values at the highest level of the MSM. Since $w \equiv 0$ at the top boundary of the MSM, continuity and this condition of horizontal uniformity infer that $w \equiv 0$ at all the added points. Thus, the flow in the added levels is uniform and horizontal.

The potential temperature θ is defined by extending the existing vertical gradient upward at the top of the MSM. The mixing ratio q_v in a column is held fixed at its value on the top level of the MSM. Since relative humidities are generally less than 1% at this height and the temperature is nearly constant above this level, there is no danger of developing a high-relative-humidity layer with this procedure. Cloud-water q_c and rainwater q_r are set to zero, as at lower levels.

2) BOUNDARY FORCING

The means of supplying time-dependent lateral boundary forcing to the CLM was kept simple for this study. A more sophisticated scheme may be necessary in future studies when the CLM is located farther from the MSM boundaries, but for this study, a Newtonian damping term included in the prognostic equations of the CLM is adequate to supply the forcing. The term is applied to the u, v, w, θ, and q_v equations at each time step, at the boundary points for the normal velocities, and at the point outside the boundary for the other variables. The term is of the form

$$-\alpha(S_c - S_m), \tag{4}$$

where α is a relaxation coefficient and S_c and S_m are the values of the variable at the lag time step in the CLM and MSM, respectively. The value of S_m for a given time step is obtained by linear interpolation of the time series of hourly values of the variable in the MSM. A 1-h time resolution of the boundary forcing is relatively long compared to the time scale of the convection; however, the advantage of this resolution is that high-frequency oscillations, which may be present in the MSM simulation, are not imposed on the CLM.

After testing values of α between 10^{-2} and 10^{-6}, a value of 10^{-3} was chosen. It was found that little forcing from the MSM was felt in the CLM with $\alpha = 10^{-5}$ or $\alpha = 10^{-6}$, and convection failed to develop. For $\alpha = 10^{-2}$, excessive convergence near the inflow boundaries produced spurious cloud development in this area. Values of 10^{-3} and 10^{-4} produced reasonable behavior; however, with $\alpha = 10^{-4}$, the convection was too weak. Also, the relaxation time scale of 15 min (10^{-3}) is more consistent with the model response time for this problem than is 150 min (10^{-4}).

This technique allows the CLM boundaries to respond to both the CLM and MSM. The scheme does not force the CLM to instantaneously adjust to the mesoscale flow, but it allows strong forcing from within the CLM to maintain deviations from the MSM solution. If the two models produce the same flow, the term becomes zero.

4. Initial conditions for the CLM

The initial state of the CLM at 0100 UTC 11 April is taken from the MSM after 13 h of integration. In this section, this initial state is compared with corresponding observational data to determine how the observations and model state differ.

a. Surface and boundary-layer data

The primary sources of surface observational data are the hourly Service A teletype reports. Fields of surface temperature, mixing ratio, pressure, and winds at 0100 UTC have been generated from this dataset and are shown in Fig. 4. The figure shows only the CLM

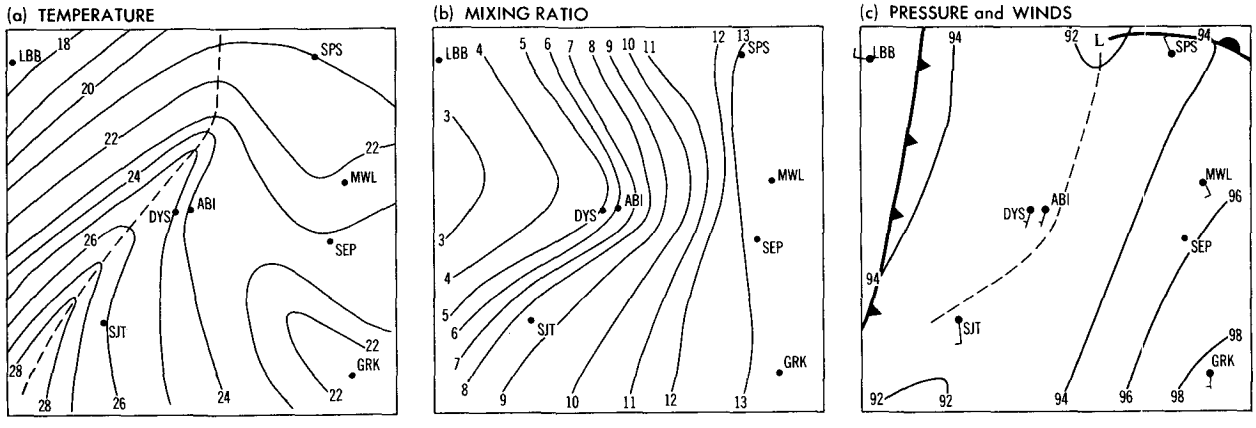

FIG. 4. Observed surface fields of (a) temperature (°C), (b) mixing ratio (g kg^{-1}), (c) pressure (hPa, only the last two digits shown) and winds (m s^{-1}) at 0100 UTC 11 April 1979 within the domain of the cloud model. Dashed line in (a) is the thermal ridge axis; dryline and cold front are indicated in (c).

domain to facilitate comparison with the model data, although data from exterior points were used in the analysis. Note that only seven observing stations (SPS, ABI, LBB, SJT, MWL, GRK, and DYS) and one radar site (SEP) are located within the domain, compared to the model's 6400 grid points. Thus, small-scale model features cannot be verified because of the inadequate resolution of the observations.

The observed surface data is compared with MSM data at the lowest level (243 m) at 0100 UTC 11 April (Fig. 5). This level is rather far from the surface but should be adequate for a comparison of large-scale features. The primary difference to be noted between the observations and model fields is the displacement of the dominant model features to the west of their observed positions. Note also, the comparable magnitudes of the variables and the more concentrated gradients in the model compared to the observations. Only the wind speeds differ significantly between model and observations. Model winds at 243 m above the surface are generally 20–30 m s^{-1}. However, the highest wind gusts observed at the surface are only 15 m s^{-1}, suggesting that the actual winds at 243 m may be much less than 30 m s^{-1}.

b. *Upper-level data*

At upper levels, analyses of observed radiosonde data are available only at 3-h intervals (i.e., 0000, 0300, and 0600 UTC). Comparisons (not shown) were made between model data at 0100 UTC and observations at 0000 UTC, the closest available observation time. As at the surface, the dominant features at upper levels in the model are found to the west of their observed locations, and model wind speeds are, on average, too strong by 10–15 m s^{-1}. However, the large-scale pattern of the features in the model's initial condition resembles the analyzed observations.

The satellite picture at 0101 UTC, shown in Fig. 2b, and radar data from the MAF and SEP radar sites also provide information on the actual state of the atmosphere at 0100 UTC. The satellite picture shows a narrow cloud band just west of ABI and SJT that had been growing slowly for several hours. Precipitation was first detected on radar about 0130 UTC, suggesting that at 0100 UTC the clouds were probably in the cumulus-congestus stage of development. In the MSM simulation, no cloud is present in the region of the observed cloud line. An examination of the vertical motion fields in the area shows that vertical velocities are over 1 m s^{-1} at 850 mb and in excess of 0.5 m s^{-1} at 6 km. However, the air in this region is extremely dry, with relative humidities in the ascending air less than 40% throughout the lower troposphere. Thus, there seems to be a forcing mechanism for the observed clouds, but the upward motion is too weak and the air is too dry for the model to produce saturation by 0100 UTC.

c. *The convective environment*

Bluestein and Jain (1985) showed that the thermodynamic and wind characteristics of a given environment are indicators of the type of squall-line development that is likely to occur there. Examination of mean wind, temperature, and moisture soundings for both the observed state and the model's initial state will show which type of squall line is favored in this study and whether the model and observations favor the same type.

The hodographs for both the analyzed SESAME data at 0000 UTC and model conditions at 0100 UTC are shown in Fig. 6. Here v is aligned along the squall line, and u is the speed relative to the squall line, as in Fig. 14 of Bluestein and Jain (1985). The major differences noted between the SESAME and model hodographs are the much stronger low-level shear in the cross-line

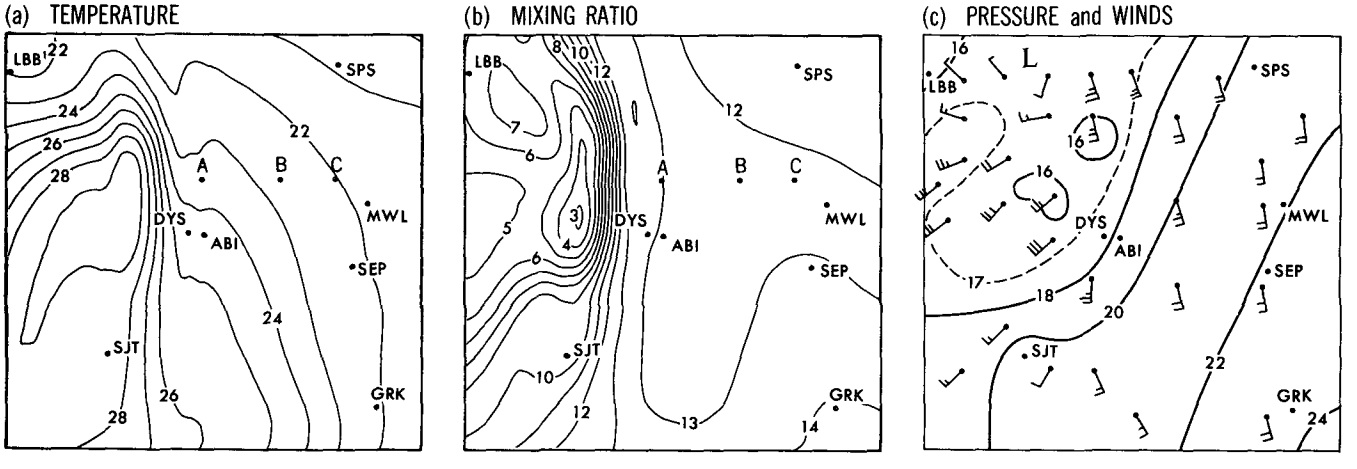

FIG. 5. As in Fig. 4, but at the lowest model level (243 m) in the MSM simulation at 0100 UTC 11 April 1979. Letters (*A–C*) in (a) and (b) denote points for which time series are shown in Fig. 12.

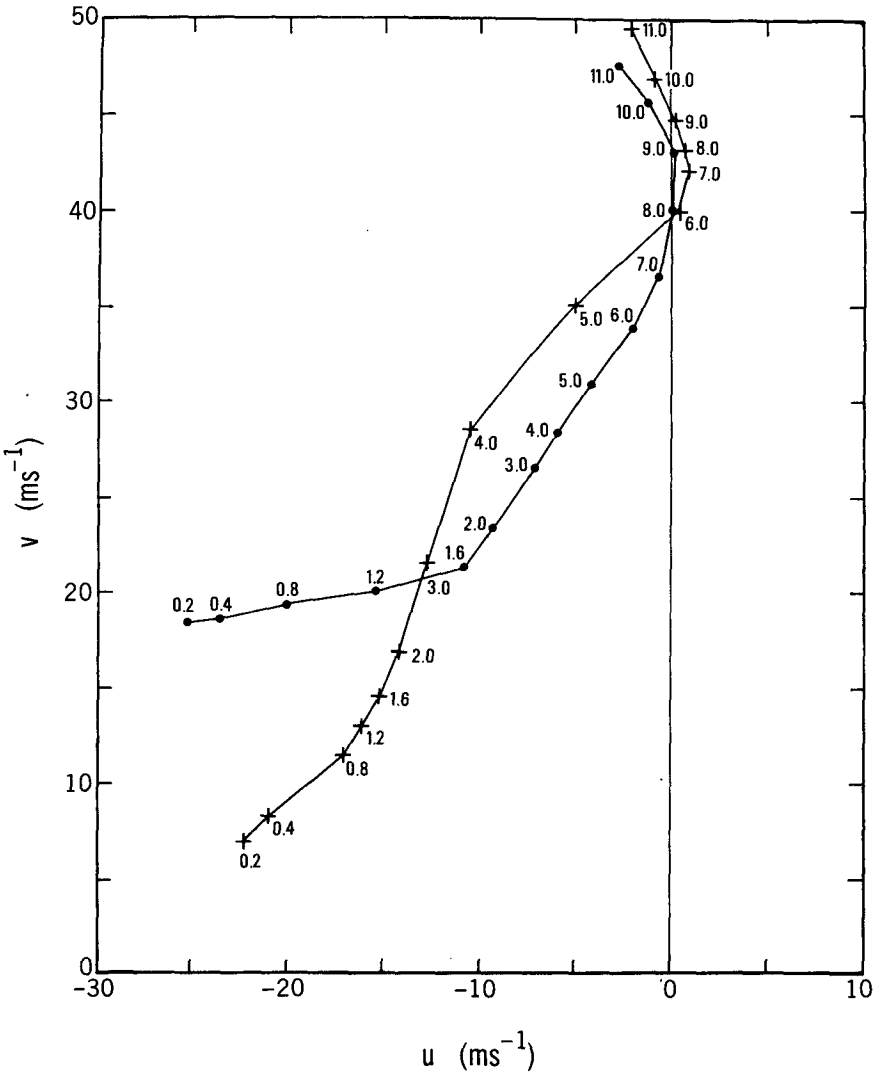

FIG. 6. Mean hodographs for the analyzed SESAME winds at 0000 UTC and for the initial model wind fields at 0100 UTC in the region in which the squall line develops. Wind component u is the relative flow normal to the line and v is the flow along the squall line. Circles represent SESAME sounding while crosses represent the model winds. Numbers indicate height above ground (km) of the given velocity.

direction and the stronger along-line wind speeds below 4 km found in the model. Above 2 km, the general shape of the hodograph is similar, with the model hodograph having less shear than the analyzed data in this region. Although there is a significant difference between the hodographs, the strong v component of the flow, the increasing u velocity with height that becomes slightly positive in upper levels, and the general shape of the hodograph between 2 and 7 km suggest a back-building line, as shown in Fig. 14b of Bluestein and Jain (1985) for both model and analyzed conditions.

Examination of a representative low-level parcel rising in this environment also suggests that a back-building squall line would be produced in this study. Large convective inhibitions (CIN) of 138 $m^2 s^{-2}$ in the observations and 157 $m^2 s^{-2}$ in the model, small bulk Richardson numbers (31 in the observations, 7 in the model) and moderate convective available potential energies (CAPE) of 1325 $m^2 s^{-2}$ in the observations and 1506 $m^2 s^{-2}$ in the model, are also signatures of the back-building line (Table 3, Bluestein and Jain 1985). These values of CIN and CAPE are calculated from the mean sounding over the entire model domain. However, values vary considerably between the hot, dry air mass in the west and the moister air mass to the east. The dry air to the west is characterized by extremely large values of CIN (300 $m^2 s^{-2}$) and very

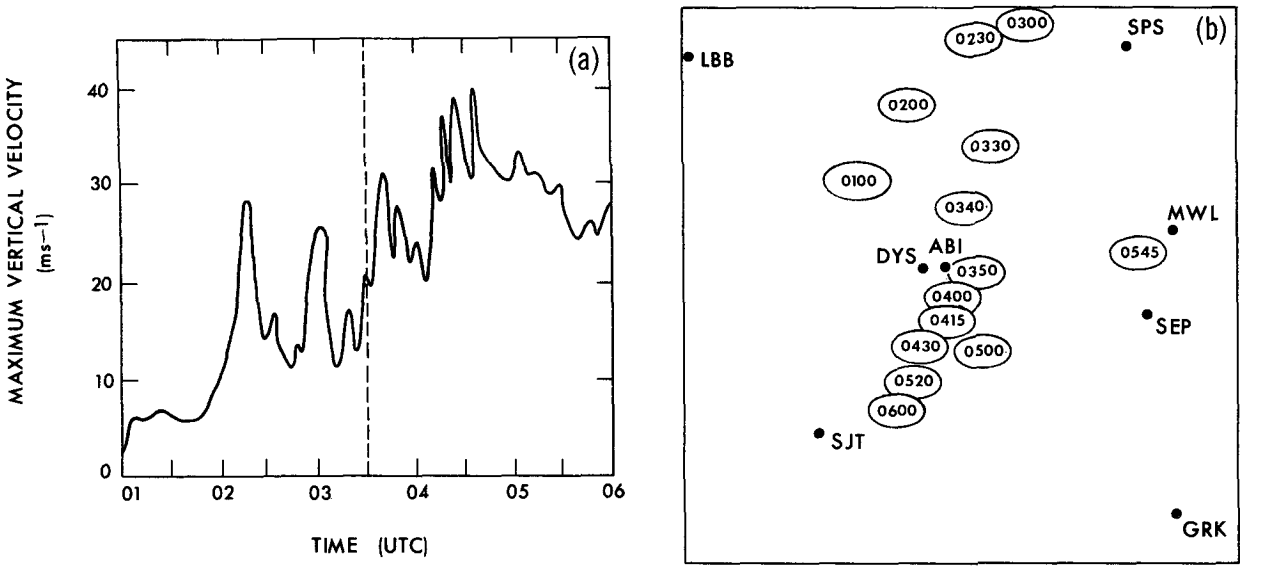

FIG. 7. (a) Maximum vertical velocity (m s^{-1}) as a function of time. Long-dashed line denotes the beginning of the squall-line stage of the simulation. (b) Location of maximum vertical velocity at various times during the simulations.

low CAPE; the absence of low-level moisture and the warm temperatures elevate the level of free convection to 600 hPa and reduce CAPE to less than 1000 $m^2 s^{-2}$. In the warm, moist air in the eastern part of the domain, CIN is smaller and CAPE is larger (1700 $m^2 s^{-2}$) as a consequence of the higher moisture content.

Thus, both observations and model initial conditions suggest the development of a back-building line. Because of the larger CIN and stronger shear in the model environment, the model may have more trouble initiating deep convection than does the analyzed environment. However, the larger values of CAPE suggest that the model convection may grow faster and ultimately be stronger once the initial inhibition is overcome.

5. The model simulation

a. The pre-squall-line stage (0100–0330 UTC)

Deep convection develops north of ABI between 0100 and 0330 UTC. At 0100 UTC, the major center of upward motion is located northwest of ABI, behind the model dryline seen in Fig. 5b. During the first hour of integration, weak convective cells form in this area and move off to the north-northeast, growing slowly. By 0200 UTC, updraft speeds in these cells have increased to 9 m s^{-1} at heights of 6–7 km, and precipitation-size particles are present within the cells, although rain has not yet fallen below cloud base. The magnitude of the maximum vertical velocity w_{max} as a function of time is shown in Fig. 7a, and the location of w_{max} at various times during the simulation is plotted in Fig. 7b.

Between 0200 and 0300 UTC, w_{max} is located north of ABI, as cells form in this area and move northeastward. Vertical velocities exceed 20 m s^{-1} in the strongest cells, which produce nearly 1 cm of rain along their paths. During this time, cells grow slowly so that

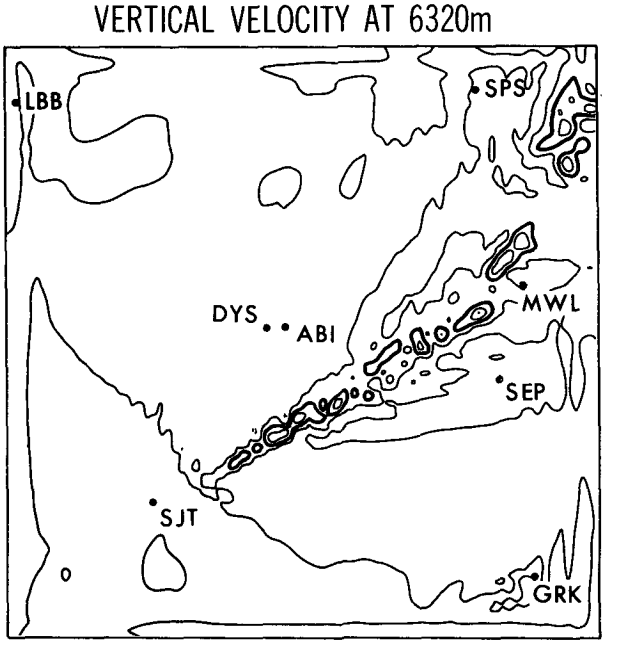

FIG. 8. Vertical velocity field at 6320 m at 0600 UTC. Heavy contours enclose values greater than the contour interval; solid lines outside of the heavy contours are zero lines. Contour interval is 3.0 m s^{-1}; maximum value is 9.09 m s^{-1}; and minimum value is −3.05 m s^{-1}.

w_{max} remains in the same cell for a long period. It is not until a cell decays significantly that w_{max} enters a newer, growing cell.

However, after 0300 UTC a change occurs. New cells begin to form and grow so rapidly that w_{max} no longer remains in a cell for an extended period; instead, as one cell is growing, a new and more rapidly growing cell forms upwind, resulting in the movement of w_{max} southwestward into the newer cell. Such growth is characteristic of back-building systems, as described by Bluestein and Jain (1985), and is suggested by satellite pictures of this squall line and the pre–squall-line environment described in section 4. This more rapid growth rate results from the consolidation of the dryline and cold-frontal convergence areas into a single, more intense convergence zone. This conclusion was reached by Ross (1987) in his study of this system with a coarser resolution grid and is again seen in the CLM simulation. By 0330 UTC, a line of cells is present between ABI and SPS, with several cells having vertical velocities exceeding 15 m s^{-1}.

b. The squall-line stage (0330–0600 UTC)

1) VERTICAL VELOCITY FEATURES

The squall-line stage of the simulation lasts from 0330 until 0600 UTC, when model integration was terminated, and is characterized by the presence of a line of deep convective cells, shown in the vertical velocity field at 0600 UTC at 6320 m (Fig. 8). As seen in Fig. 7a, the CLM maintains a vertical velocity maximum of over 20 m s^{-1} somewhere in the line during this time. Peak values of nearly 40 m s^{-1} occur at about 0440 UTC, followed by a slow decline to about 25 m s^{-1} by 0600 UTC. The strongest convective updrafts are generally located between ABI and SJT (Fig. 7b). Numerous cells form in this area and move off to the northeast, with new cells forming farther south. This is the area in which the majority of severe weather reports were received in the early stage of the squall-line system (Figs. 3b and 3c). Between 0540 and 0600 UTC, w_{max} occasionally occurs just southwest of MWL, in the area of the second set of severe weather reports, as shown in Fig. 3d. Thus, locations of extreme vertical motion in the CLM simulation correspond well with the areas of observed severe weather.

2) LIQUID WATER FIELDS

Vertically integrated liquid water fields at 0400 and 0600 UTC are shown in Fig. 9 and indicate that the liquid water area moves southeastward and expands in size between 0400 and 0600 UTC. Observed cloudiness at 0400 UTC (Fig. 3c) covers a larger area than does liquid water in the model, in part, because of the late development of the model squall line. However, by 0600 UTC the model liquid water field has become more plumelike, similar to the observed cloud cover (Fig. 3d). The back edge of the cloud shield is just east of SJT, ABI, and SPS in both the observations and in the simulation. However, the satellite picture shows cloudiness extending south of SJT at 0600 UTC, while cloudiness in the simulation remains farther north.

Liquid water maxima are correlated with high rain-

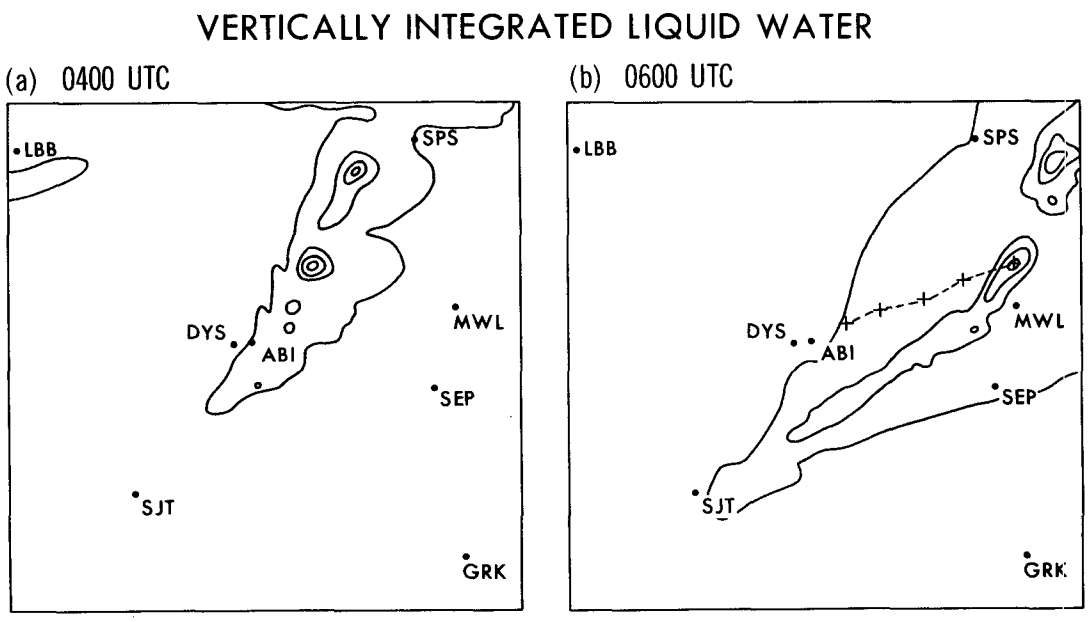

FIG. 9. Vertically integrated liquid water fields (a) at 0400 UTC, and (b) at 0600 UTC. Contours of 0, 1, 3, and 5 cm of liquid water are shown. Position of liquid water maximum at 0400, 0430, 0500, 0530, and 0600 denoted by crosses in (b).

water content. Only at the southwestern end of the line does the cloud water contribute significantly to the total liquid water; the model cloud physics rapidly converts cloud water to rainwater when rainwater is present. At 0400 UTC, rainwater is found primarily between ABI and SPS, farther north and west than shown by the radar data of Fig. 3. Much better agreement is seen at 0600 UTC in the northern part of the line, but model rainwater still is too far north and west of its observed location at the southern end of the line. Fig. 9b shows the path of one center, its position plotted every 30 min, beginning at 0400 UTC. It moves east-northeastward at about 20 m s^{-1} (39 kt), which is slightly slower than the 40–45-kt cell speeds reported in National Weather Service radar summaries.

The precipitation generated by the model between 0300 and 0600 UTC is shown in Fig. 10, along with the observed precipitation during the same period. The heaviest rain, over 5 cm, is produced in the CLM between SPS and MWL, embedded within a general area of rainfall in excess of 1.25 cm extending from east of ABI to the northeastern corner of the domain. The observed precipitation (falling between 0300 and 0600 UTC) extends northeastward from SJT to MWL and then out of the domain with a maximum value of 1.75 cm south of ABI. The model failed to produce precipitation as far south as was observed, perhaps as a result of the excessive southwesterly wind speeds noted in section 4. The heavier model precipitation may reflect both the poor resolution of the observations and overly strong model convection.

3) BOUNDARY-LAYER FEATURES

Boundary-layer features of the squall-line system are shown in Fig. 11. The 243-m temperature field at 0600 UTC (Fig. 11a) shows two temperature maxima. A very strong temperature gradient [as much as 7 K (14 km)$^{-1}$] is produced at the leading edge of the convective outflow (denoted by SL in Fig. 11a), with temperatures dropping below 16°C in the area of heavy rainfall. Upwind of the rain area temperatures warm to their pre–squall-line value (24°C) before dropping again behind the model cold front (CF in Fig. 11a).

The vertical velocity field at 487 m (Fig. 11b) shows a line of concentrated upward motion extending for nearly 400 km from near SJT northeastward past MWL. Downdraft–updraft couplets extend southwestward over 300 km from the northern end of the line, indicating the region over which precipitation is occurring.

The mixing ratio field (Fig. 11c) shows that the dry air behind the squall line has advanced farther east in the central part of the line (west of MWL) where the falling rain has produced strong evaporatively driven outflow and has weakened the horizontal moisture gradient. North of MWL, heavy rain and evaporation have raised mixing ratios to 14 g kg^{-1}, values that are otherwise confined to an area near the southern boundary. At the southwestern end of the line, the initially dry air has not been moistened by rainfall, but the combination of the eastward movement of the dry air and the advection of moisture northward ahead of

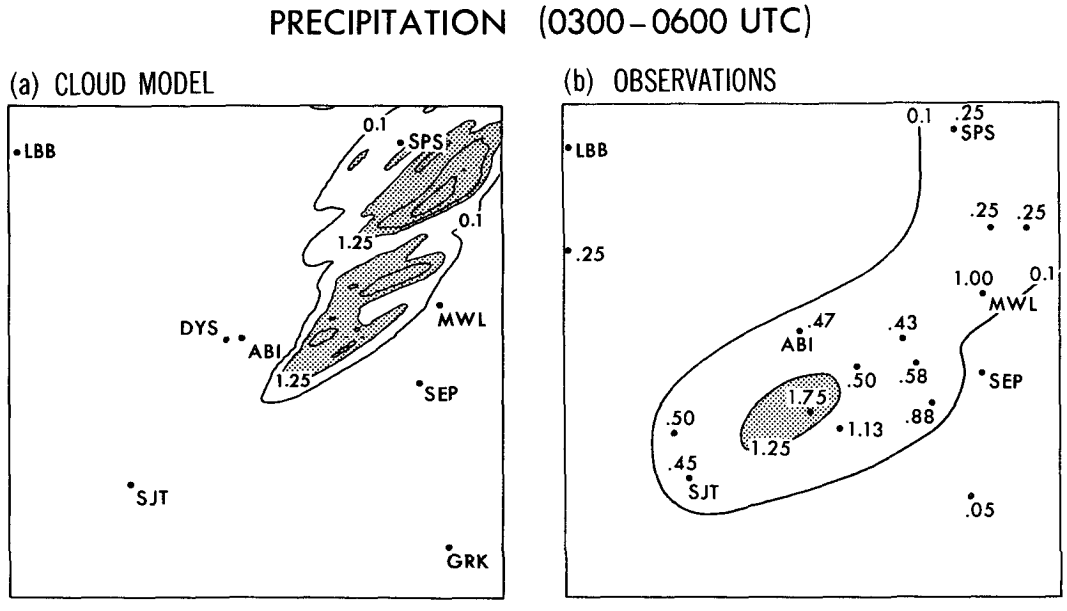

FIG. 10. Precipitation (cm) falling between 0300 and 0600 UTC 11 April from (a) CLM simulation, and (b) observations from *Hourly Precipitation Data* (National Climatic Center 1979). Contours are 0.1, 1.25, 2.5, and 5.0 cm; areas with over 1.25 cm of precipitation are stippled.

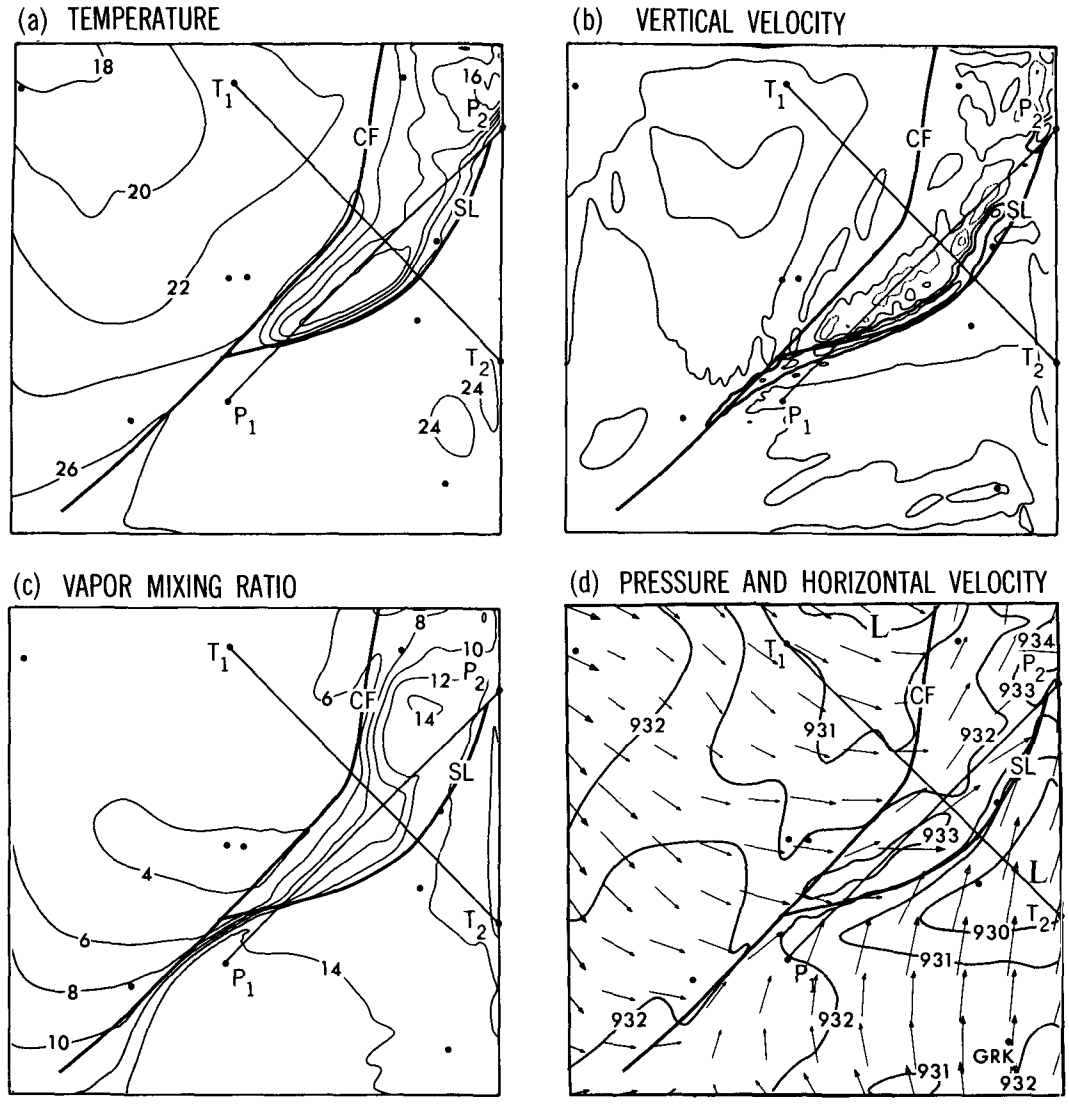

FIG. 11. Model fields at 0600 UTC. (a) Temperature (°C) at 243 m above the surface. Observing stations shown in Fig. 8 are indicated by dots. Line segments P_1P_2 and T_1T_2 denote the positions of the cross sections shown in Figs. 14–16; heavy solid lines labeled CF and SL denote the locations of the cold front and leading edge of the squall line. (b) Vertical velocity field at 487 m. Negative contours are dotted. Contour interval is 0.6 m s^{-1}; maximum value is 1.47 m s^{-1} and minimum value is −1.04 m s^{-1}. Areas of upward motion over 0.6 m s^{-1} are enclosed in heavy contour. (c) As in (a), but for vapor mixing ratio (g kg^{-1}) at 243 m. (d) As in (a), but for pressure (hPa) and horizontal wind fields (m s^{-1}).

the line has intensified the horizontal moisture gradient. This is the region where new deep convective cells are generated. With over 13 g kg^{-1} of low-level moisture and temperatures near 26°C, values of CAPE in this area now exceed 2500 m^2 s^{-2} while CIN approaches zero, allowing large vertical velocities to quickly develop in these cells.

Low pressure centers are located along the northern boundary west of SPS and also south of MWL (Fig. 11d). The two low centers are separated by a pressure ridge coincident with the falling precipitation, with a pressure maximum near the northeastern corner of the grid. Pressure is over 3 hPa higher in the squall line than just ahead of it and then drops 1–2 hPa to its rear. Such a pressure pattern is typical of a squall-line system. The horizontal wind fields at 0600 UTC (Fig. 11d) show a wind shift at both the squall line and cold front. Peak west winds near 20 m s^{-1} are found along the gust front.

4) "WEATHER": MODELED AND OBSERVED

It is also of interest to look at various "weather" variables at model points as a function of time to see

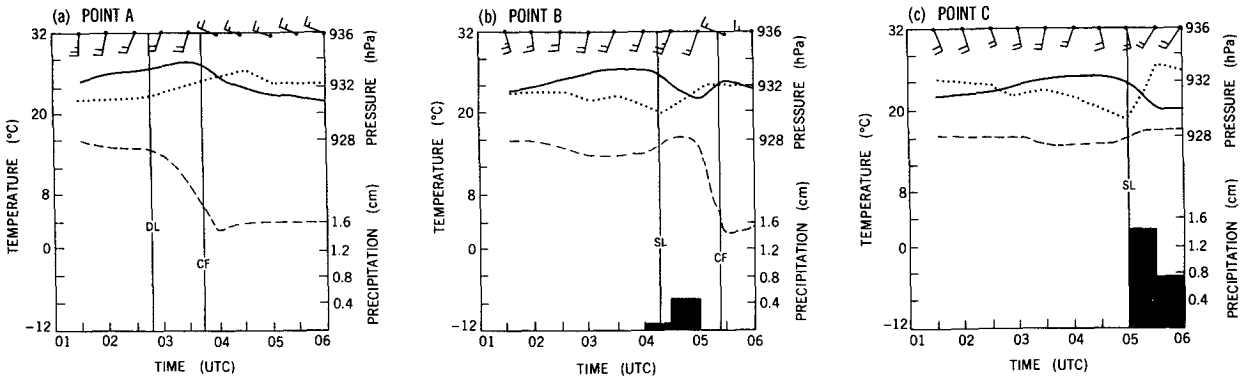

FIG. 12. (a)–(c) Time series of pressure (hPa, dotted line), temperature (°C, solid line), dewpoint temperature (°C, dashed line), wind speed (m s^{-1}) and direction, at a height of 243 m, and precipitation (cm), at points (*A–C*) of Fig. 5, respectively. Times of dryline, squall-line and cold-frontal passage are indicated by DL, SL, and CF, respectively.

how the passage of the model dryline, squall line, and cold front would be seen from the point of view of an observer at a fixed point on the ground. Since there is no surface data in the model, variables at 243 m will be used for this exercise. Three model points were selected; the locations of these points, denoted *A–C*, are shown in Fig. 5.

Figure 12 shows the time series of pressure, temperature, dewpoint, vector wind, and precipitation at these stations during the model integration. Also indicated are times of cold-frontal (CF), dryline (DL), and squall-line (SL) passage at each station. Approach and passage of the dryline at point *A* produced a veering of the winds toward the southwest, rising temperatures, and falling dewpoints. Passage of the cold front at points *A* and *B* resulted in a temperature fall and a shift of the winds to the northwest with a slow diminishing of intensity. As the squall line approached points *B* and *C*, the pressure fell; with its arrival, the pressure rose rapidly and then leveled off, the temperature fell rapidly, winds increased in speed from the southwest, and rain fell heavily. These characteristics are more pronounced at point *C* than at point *B*, since the squall line was more highly developed as it approached point *C*. The end of the precipitation at point *B* was followed by rising temperatures and falling dewpoints ahead of the approaching cold front.

The limited surface observations also suggest many of these features. Figure 13 shows a time series of surface observations from LBB and ABI. The dryline passage at about 1900 UTC at LBB was accompanied by a temperature rise and a rapid fall of the dewpoint. Frontal passage occurred between 2300 and 0000 UTC and was characterized, as in the model, by a temper-

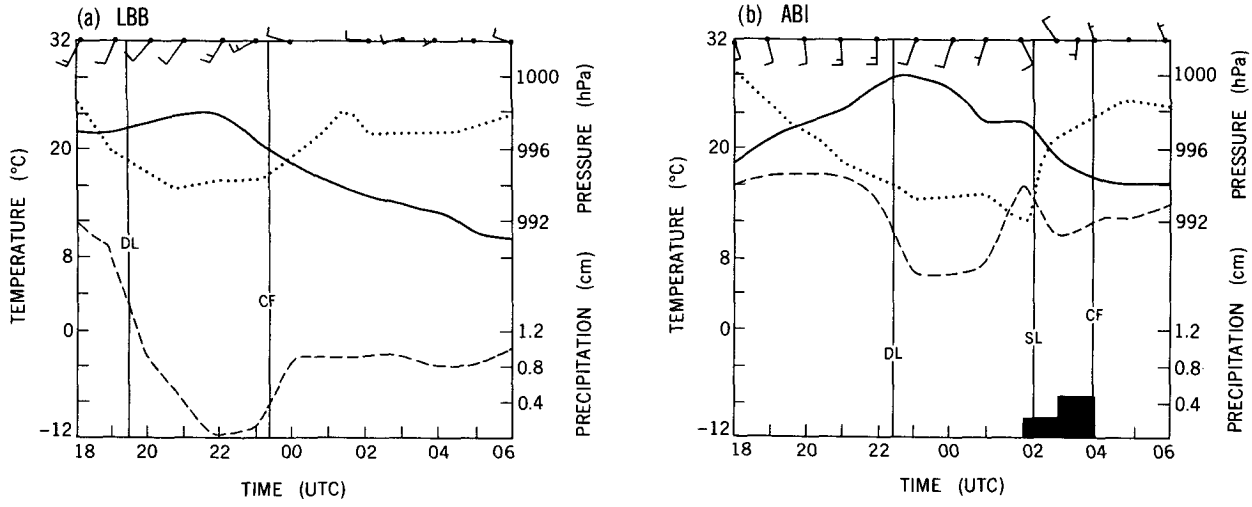

FIG. 13. Time series of surface observations, i.e., altimeter setting (hPa, dotted line), temperature (°C, solid line), dewpoint temperature (°C, dashed line), wind speed (m s^{-1}) and direction at (a) Lubbock (LBB) and (b) Abilene (ABI) between 1800 UTC 10 April 1979 and 0600 UTC 11 April 1979. Passage of dryline, squall line, and cold front are indicated by DL, SL, and CF, respectively.

ature drop and a wind shift to the northwest. Surface pressure and dewpoint temperature also rose behind the front and then leveled off.

The observations from ABI also show features consistent with the model. Arrival of the dryline at ABI occurred between 2200 and 2300 UTC resulting, as at LBB, in rising temperatures, falling dewpoints, and a veering of the winds. Falling pressure, backing winds, and rising dewpoints signaled the approach of the squall line, which arrived just after 0200 UTC. Pressure rose as the rain began, the temperature dropped, and the winds became variable during the period of rain, which lasted for approximately 1.5–2 h and produced a total of 0.7 cm. Data are not available to indicate whether the end of the rainfall was marked by rising temperatures and falling dewpoints. After cold-frontal passage (about 0400 UTC), the temperature and dewpoint leveled off, as the winds became northwesterly and very light.

5) Vertical cross sections: Along line and across line

The vertical structure of the squall line in the CLM is shown in Figs. 14–16, which contain cross sections both along and across the line. The sections shown are

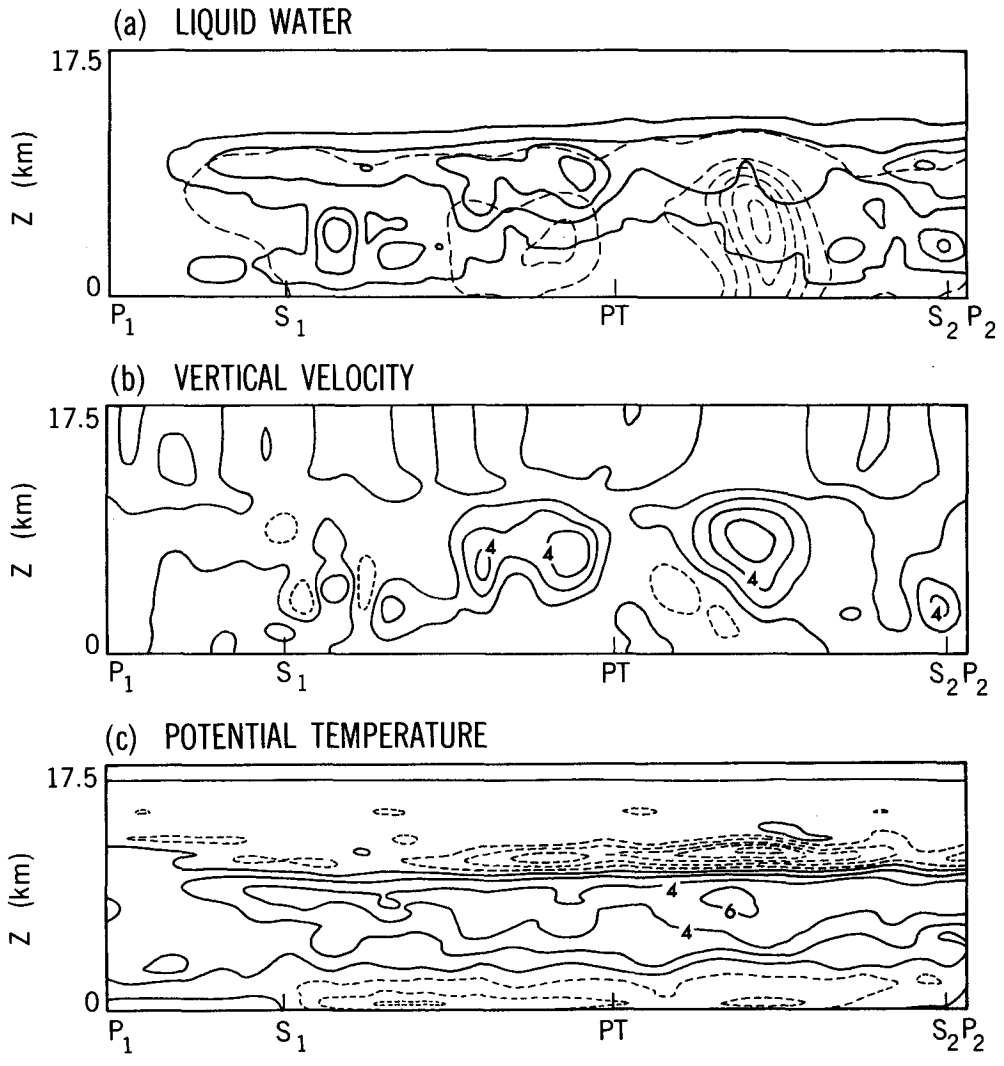

FIG. 14. Vertical cross sections along the squall-line segment P_1P_2. Note that the vertical coordinate is stretched by a factor of 5. Letters S_1 and S_2 denote the intersections of the cross section with the leading edge of the squall line. *PT* marks the intersection of P_1P_2 with T_1T_2. (a) Liquid water fields (cloud water—solid contours, contour interval of 0.25 g kg^{-1}, maximum value of 0.93 g kg^{-1}); rainwater—dashed contours, contour interval of 1.0 g kg^{-1}, maximum value of 5.28 g kg^{-1}). (b) Vertical velocity field (contour interval of 2.0 m s^{-1}, dashed contours negative, maximum value of 7.07 m s^{-1}, minimum value of −3.62 m s^{-1}). (c) Disturbance potential temperature (contour interval of 2.0 K, dashed contours negative, maximum value of 6.3 K, minimum value of −10.6 K).

identified by the line segments P_1P_2 (parallel to the line) and T_1T_2 (transverse to the line) in Fig. 11.

The cross section along the line (Fig. 14) shows that the squall line has a deep cloud layer (the cloud top is just under 12 km) over nearly the entire 311-km region shown. Local maxima of cloud water are located in the two areas where the section crosses the gust front (denoted by S_1 and S_2), where fairly deep upward motion is also found (Fig. 14b). Rainwater (Fig. 14a) is found over nearly as large an area as the cloud, but is concentrated in two areas; one is in the center of the line and the other, stronger center is nearer to P_2. The latter area also has both the strongest upward and downward motion (Fig. 14b), and the highest potential temperature excess and deficit (Fig. 14c) along the section shown, and is in the area of the vertical velocity maximum near MWL (Fig. 7b).

Broad areas of upward motion are found in the middle atmosphere over most of the section, with sinking motion more prevalent at the southern end, and immediately adjacent to the strong cells. The potential temperature field indicates that relative cooling of 2–

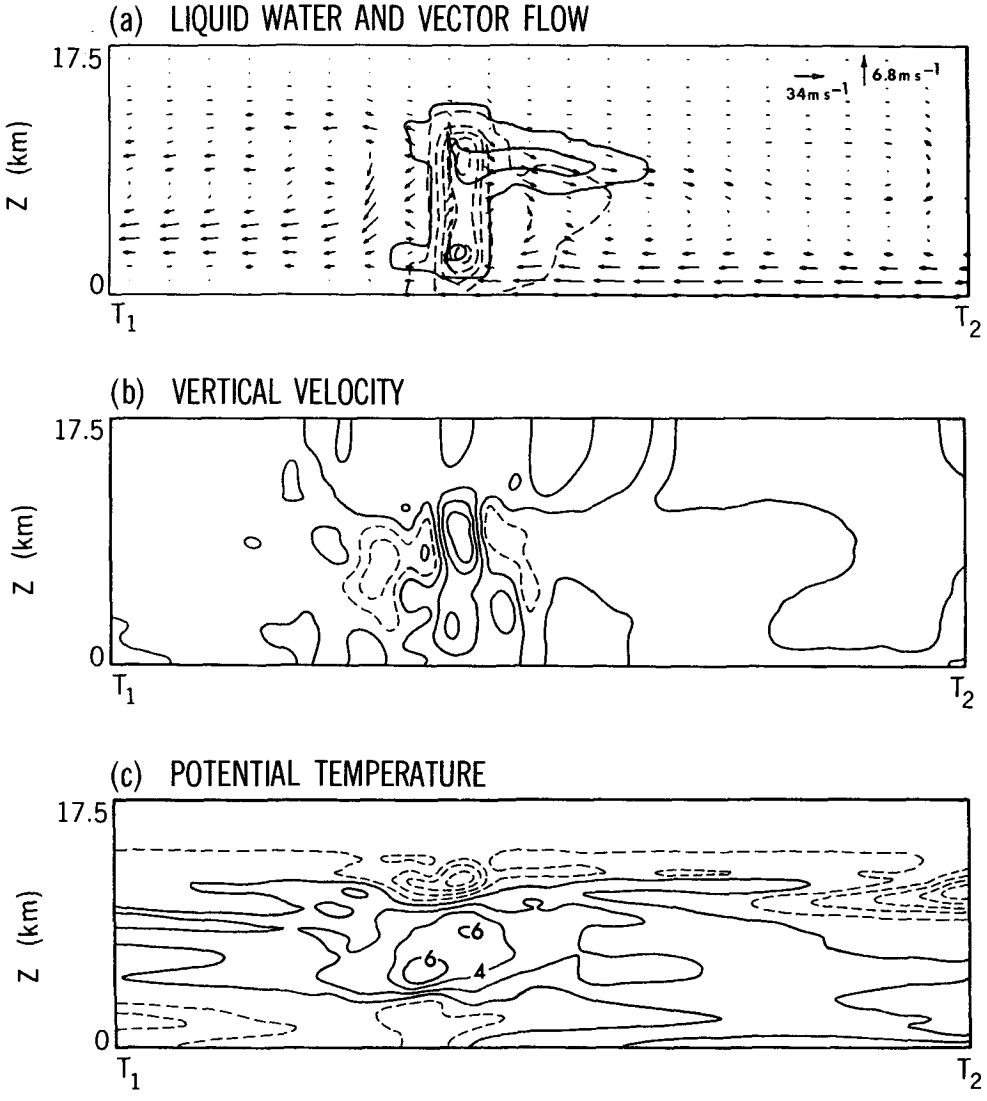

FIG. 15. As in Fig. 14, but sections transverse to the squall line along segment T_1T_2 at 0430 UTC. (a) Liquid water fields (cloud water—solid contours, contour interval of 0.25 g kg^{-1}, maximum value of 0.40 g kg^{-1}); rainwater—dashed contours, contour interval of 0.5 g kg^{-1}, maximum value of 2.00 g kg^{-1}) and velocity vectors relative to the squall line. (b) Vertical velocity field (contour interval 1.25 m s^{-1}, dashed contours negative, maximum value of 4.73 m s^{-1}, minimum value of −3.46 m s^{-1}). (c) Disturbance potential temperature (contour interval of 2.0 K, dashed contours negative, maximum value of 7.35 K, minimum value of −10.63 K).

4 K is generally present below 3 km, resulting from evaporational cooling in the area of falling rain. Condensational warming is found from the top of this layer to approximately 10 km, with a layer of maximum warming of over 4 K between 7 and 9 km. Strong cooling takes place near cloud top as a result of convective overshoot and evaporation, with a maximum potential temperature deficit of 10 K above the strongest updraft.

Transverse sections at 0430 UTC (Fig. 15) and at 0600 UTC (Fig. 16) show the evolution of the developing squall line. At 0430 UTC, a nearly vertical updraft with cloud- and rainwater spreading downshear is present. The vertical velocity pattern (Fig. 15b) shows two centers of upward motion in the cloud (one at upper levels and the other just above cloud base) associated with the two maxima in rainwater seen in Fig. 15a. Sinking motion is seen on either side of the cloud with a gyrelike circulation ahead of the line, and strong sinking and accelerated rearward flow behind the line. Low-level flow approaches the line from the front, with anvil outflow to both the front and rear. Cooling is found in the area of falling rain and near cloud top, while warming is present in the convective updraft.

By 0600 UTC (Fig. 16), the flow has evolved into

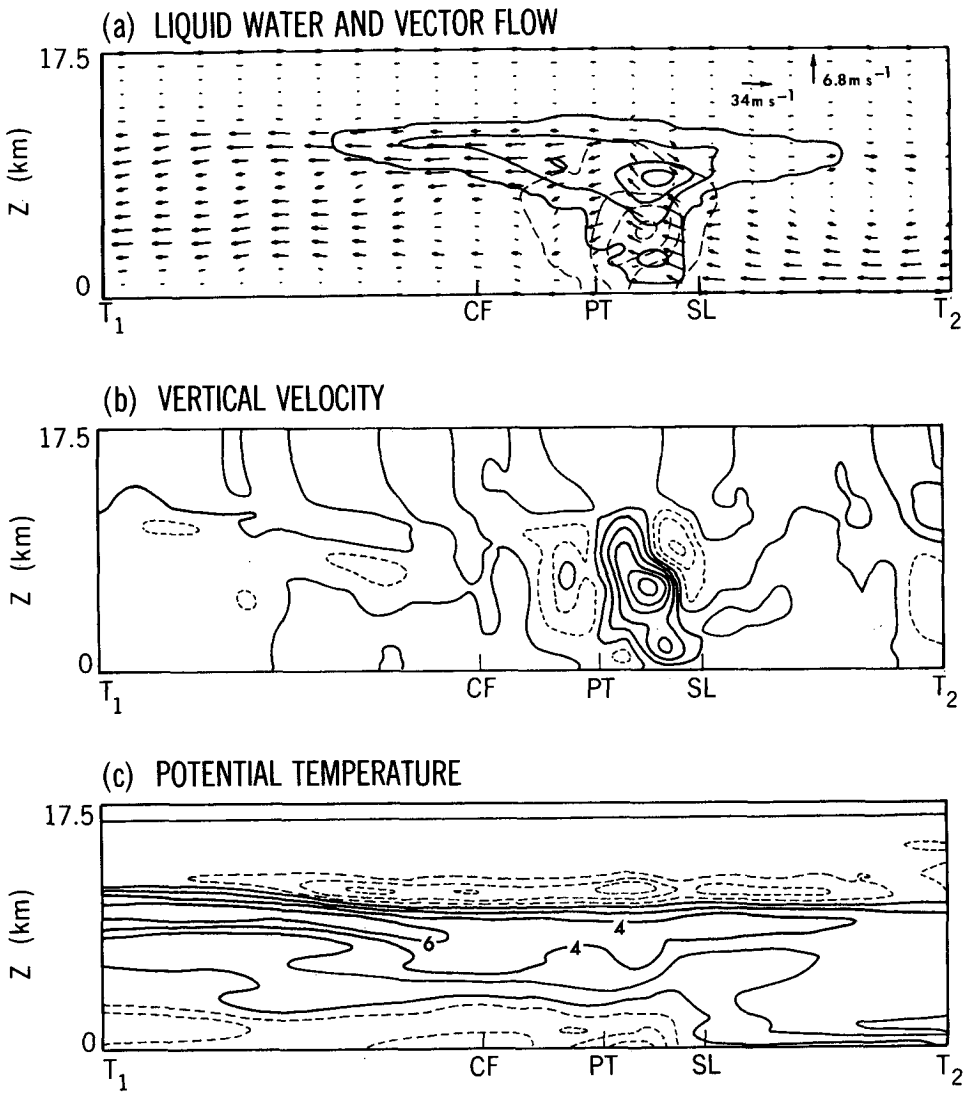

FIG. 16. As in Fig. 14, but sections transverse to the squall line along segment T_1T_2 at 0600 UTC. CF is the position of the cold front, and SL denotes the leading edge of the squall line. (a) Liquid water fields (cloud water—solid contours, contour interval of 0.25 g kg^{-1}, maximum value of 0.83 g kg^{-1}); rainwater—dashed contours, contour interval of 0.5 g kg^{-1}, maximum value of 1.58 g kg^{-1}) and velocity vectors relative to the squall line. (b) Vertical velocity field (contour interval of 0.5 m s^{-1}, dashed contours negative, maximum value of 2.69 m s^{-1}, minimum value of -1.51 m s^{-1}). (c) Disturbance potential temperature (contour interval of 2.0 K, dashed contours negative, maximum value is 7.97 K, minimum value is -7.88 K).

a slightly upshear tilting system, with most of the anvil found to the rear of the updraft. Precipitation is falling in a narrow band 36 km wide, and rainwater aloft is also confined to the immediate vicinity of the squall line. Deep updrafts are found in the squall line (Fig. 16b). Downdrafts behind the line penetrate to the surface, and the sinking ahead of the line is confined above 4 km. A deep layer of weak updraft is found ahead of the squall line, with upward motion extending as high as 10 km about 50 km ahead of the line. Behind the squall line, there is a deep but weak updraft produced by convergence of outflow and the flow ahead of the approaching cold front, followed by a region of shallow updrafts overlain by very dry (less than 10% relative humidity) and warm (Fig. 16c) air that is sinking under the anvil. The maximum disturbance potential temperature in the cross section is found in this region under the anvil.

Warm, dry air (relative humidity of less than 20%) is also found well ahead of the squall line in a layer between 1 and 8 km. This air is the remnant of the hot, dry air mass initially seen in the southwestern portion of the domain (Fig. 4), which has moved eastward over the cooler surface air.

In low levels, strong evaporative cooling is found just behind the squall line, with warmer temperatures farther to the rear where the rainfall and accompanying evaporation is less intense (Fig. 16c). Weaker cooling is associated with the cold front. Also shown is the cooling near and above cloud top resulting from forced uplift and evaporation of cloud droplets.

6) COMPARISON WITH A 20-KM HORIZONTAL RESOLUTION SIMULATION

In addition to the 5-km horizontal resolution simulation reported here, a simulation using 20-km horizontal resolution, the same as the resolution of the MSM, was carried out. It was found that at this resolution the CLM could not produce a multicelled squall line as seen in Fig. 8; only a single deep cell is present in the northeastern corner of the domain at 0600 UTC, as seen in Fig. 17a. This cell had originated in the region northeast of ABI around 0400 UTC and moved northeastward during the following 2 h.

A similar lack of development of multiple cells is seen at 243 m (Fig. 17b). Here there is a downdraft maximum associated with rainfall from the deep cell and updraft centers nearby where the outflow from the cell converges with the ambient flow. An area of weak upward motion extends in a line southwestward from the cell, but this feature fails to show any development. Thus, the use of 20-km resolution and the accompanying loss of nonhydrostatic effects leads to a change in the nature of the simulation from a multicelled squall line to a single deep convective cell.

7) COMPARISON WITH A 2-KM MODEL SIMULATION WITH SIMILAR SHEAR

A recent study by Weisman et al. (1988), hereafter referred to as WKR, on the effects of variations of vertical wind shear on the structure and evolution of squall

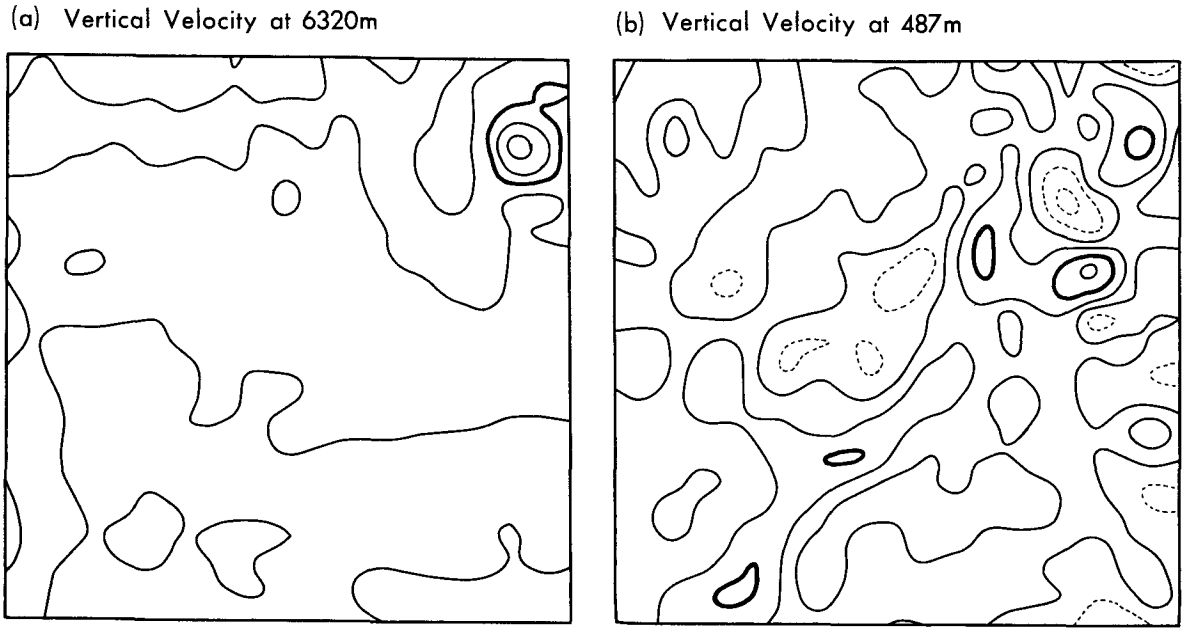

FIG. 17. Vertical velocity field at 0600 UTC at (a) 6320 m and (b) 487 m. For (a) contour interval is 1.5 m s^{-1}; areas with upward motion exceeding this are enclosed by the heavy contour. For (b) contour interval is 0.1 m s^{-1}; areas of upward motion exceeding 0.2 m s^{-1} are enclosed within the heavy contour. Extreme values are for (a) 4.98 and −0.77 m s^{-1}, and (b) 0.34 and −0.24 m s^{-1}.

lines indicates how squall lines evolve in different ambient wind-shear conditions. The environment in the present study has strong shallow shear (16 m s^{-1} in the bottom 2 km) overlain by a weaker shear of approximately 9 m s^{-1} over the next 5 km (Fig. 6). Since the shear in the lowest levels and in the direction normal to the line is most important in determining the squall-line characteristics (WKR), comparison with their case of 17.5 m s^{-1} of shear over 2.5 km, shown in their Figs. 7 and 11, is appropriate.

Although many details of the flow differ, many similarities of the large-scale features are seen when the present case is compared with that of WKR. The cloud outlines in Figs. 15 and 16 are similar to those at 2 and 4 h in Fig. 7 of WKR, showing the evolution from a largely upright cloud with a forward anvil to a cloud with slight upshear tilt and a larger rear anvil. In both studies, relative inflow occurs at low- and midlevels at the front of the system with rearward anvil-level outflow increasing with time. Both cases still have significant updrafts at the final time, although both have entered a stage of slow decay. And, the shift of the main updraft rearward of the gust front as the system develops upshear tilt is also seen in both studies.

Rotunno et al. (1988) introduced the ratio of the speed of the cold-air outflow (c) to the low-level environmental shear (Δu) as an indicator of the ability of the system to maintain itself via deep-cell regeneration at the gust front. Values of $(c/\Delta u)$ of order 1 represent an optimal state where the positive horizontal vorticity of the environmental wind shear is balanced by the negative horizontal vorticity associated with the horizontal buoyancy gradient along the leading edge of the cold outflow. Weisman et al. (1988) examined this ratio for the cases they studied and found that values of $(c/\Delta u)$ of order 1 for shallow shear were associated with the strongest, most long-lasting systems, while significantly larger values were associated with weaker cells that tilted upshear.

In the current study, values of $(c/\Delta u)$, calculated as in WKR, ranged from about 1 at 0430 UTC to 1.35 at 0600 UTC. These values are consistent with the values found by WKR in their case with similar shear and shows the evolution from upright cells to a slowly weakening upshear tilted stage as $(c/\Delta u)$ becomes larger than 1. Thus, the squall-line system produced with the 5-km horizontal resolution grid evolves similarly to a more idealized case with higher resolution, suggesting that the 5-km grid has captured the essential features of the life cycle of the squall line in the given wind-shear environment.

6. Concluding remarks

This study has shown that a nonhydrostatic cloud model (CLM) with 5-km horizontal resolution can produce a detailed and realistic simulation of a back-building squall line. The simulated squall line contains many features of the traditional midlatitude continental squall-line model, including strong cooling and moistening of the low-level air by evaporating rainwater, the pressure fall preceding the squall line and pressure rise upon its arrival, and characteristic wind accelerations. Additionally, the life cycle of the squall line is similar to that of a 2-km-resolution simulation with similar vertical wind shear, suggesting that the 5-km grid has captured the significant features of the convection. The 5-km resolution used in this study is still too coarse to fully resolve the convective cells, but their movement and location, particularly in the last hour of the integration, compares favorably with observations. Many of the observed variations in surface "weather" associated with this particular squall-line system are also reproduced by the model.

The most significant shortcoming of the study is the 2–3-h time lag in squall-line development, which was found in all simulations made during the course of this study. Both model deficiencies and a lack of proper forcing may contribute to this problem. The SESAME dataset at 0000 UTC 11 April contains no evidence of the cloud line seen in the satellite picture 1 h earlier. Apparently the feature that produces the initial line of cumulus congestus is of smaller scale than can be resolved in the 1° resolution SESAME dataset. As a consequence, forcing for the cloud line is likely absent or weak in the boundary forcing for the MSM, and the models are unable to initiate the cloud line. It is possible that improvements in both the MSM and CLM (such as inclusion of orography and more realistic boundary-layer effects) and higher horizontal resolution in the CLM may permit the CLM to generate the initial cloud line. However, an enhancement of the SESAME dataset to reflect smaller-scale features preceding the squall line may also be required. To determine which of these factors are most important in simulating the proper timing of the squall-line development is a goal of future research.

Several other areas remain for future work. A similar simulation has been carried out for a 400 × 400 km^2 domain in west-central Oklahoma on the same day. This area also experienced severe convection, but in the form of supercells rather than as a squall line. Analysis of this simulation will be carried out and a comparison of the model features of the squall line and supercell convection attempted. More detailed analysis of the energetics and water budget will also be made for the current study and will be compared with similar statistics from the northern simulation.

The next anticipated model improvement is to include realistic orography rather than the flat lower boundary of the current study. An upgraded surface physics package may also be developed with the aim to better account for surface heat, moisture, and momentum fluxes. Such changes may help reduce the ex-

cessive wind speeds in west Texas and produce surface "weather" more similar to what was observed.

Acknowledgments. Our thanks go to Drs. Kikuro Miyakoda, Isidoro Orlanski, and Jack Katzfey of the Geophysical Fluid Dynamics Laboratory for reviewing the manuscript and offering suggestions that improved the paper. Comments by outside reviewers also proved extremely helpful in sharpening its focus. The numerical simulations were performed on the GFDL CDC Cyber 205 computer. The gridded SESAME data were provided by Professor Dayton Vincent and Mr. Thomas Carney. The figures were prepared by Philip G. Tunison and staff, and they were photographed by John Connor.

APPENDIX A

Some Details of the Numerical Model

This appendix describes some relevant aspects of the cloud model not previously presented. Specifically, it includes discussion of the Newtonian smoother in the momentum and potential temperature equations, the bulk cloud physics parameterization, and recent modifications to the subgrid-scale formulation.

a. The Newtonian damping terms

The Newtonian damping term applied in the u, v, w, and θ equations for levels above 11.25 km is similar to the potential temperature damper discussed in LH86. It is given by

$$\left.\frac{\partial \rho_0 S}{\partial t}\right|_{\text{Newt}} = -0.2 \times 10^{-5} \rho_0 (z - z_0)(S - \langle S \rangle), \quad \text{(A1)}$$

where $z_0 = 11.25$ km, $\langle\ \rangle$ denotes the horizontal mean, and S is either u, v, w, or θ. Thus, at 17.25 km the damping constant is about 80 s. This term has been added to the momentum equations, in addition to the potential temperature equation in order to more consistently damp the gravity waves that may be in the stratosphere, having been excited by reflection from the rigid upper boundary.

b. The bulk cloud physics formulation

The formulations for the cloud physics terms generally follow Kessler (1969) or Liu and Orville (1969) and are similar to the forms shown in LH82. Specifically, the expressions are:
the fall velocity V_T

$$V_T = 5.32(\rho_0 q_r \times 10^3)^{0.2}\left(\frac{\rho_{00}}{\rho_0}\right)^{0.5};$$

$$\rho_{00} = 1.20416 \text{ kg m}^{-3}, \quad \text{(A2)}$$

autoconversion A_a

$$A_a = 10^{-3}(q_c - 1.5 \times 10^{-3}\, \rho_0^{-1}), \quad \text{(A3)}$$

collection A_c

$$A_c = 3.274 q_c (\rho_0 q_r)^{0.95}\left(\frac{\rho_{00}}{\rho_0}\right)^{0.5}, \quad \text{(A4)}$$

evaporation of rain E

$$E = 0.0486(q_{v_s} - q_v)(\rho_0 q_r)^{0.65}, \quad \text{(A5)}$$

and precipitation rate P

$$P = \left.\frac{\rho_0 V_T q_r}{\Delta z}\right|_{z=\Delta z/2}. \quad \text{(A6)}$$

The primary difference from the LH82 forms is the inclusion of the density weighting in the fall velocity term, a consequence of reduced air resistance to the falling drops at higher elevations. This effect appears in both the fall velocity V_T and the raindrop collection A_c. Additionally, a correction to the collection formula involving an additional factor of $\rho_0^{0.95}$ has been made.

c. Subgrid-scale parameterization changes

For this study, the eddy diffusivity K_h is set equal to the eddy viscosity K_m, rather than being three times larger as in LH88. It has been found that with a horizontal grid interval of 5 km the use of $K_h = 3K_m$ leads to excessive mixing and severely inhibits the development of new clouds. By setting K_h equal to K_m, mixing of the thermodynamic fields is reduced, allowing more opportunity for the clouds to develop (Wilhelmson and Chen 1982).

Because of the different horizontal and vertical grid intervals, changes were made in the formulations of the components of the Reynolds stress. Equation (A7) of LH88 is replaced by

$$\tau_{11} = \rho_0 K_m\left[2\frac{\partial u}{\partial x}\left(\frac{\Delta x}{\Delta}\right)^2 - \text{DIVM}\right]$$

$$\tau_{22} = \rho_0 K_m\left[2\frac{\partial v}{\partial y}\left(\frac{\Delta y}{\Delta}\right)^2 - \text{DIVM}\right]$$

$$\tau_{33} = \rho_0 K_m\left[2\frac{\partial w}{\partial z}\left(\frac{\Delta z}{\Delta}\right)^2\right]$$

$$\tau_{12} = \tau_{21} = \rho_0 K_m\left[\frac{\partial u}{\partial y}\left(\frac{\Delta y}{\Delta}\right)^2 + \frac{\partial v}{\partial x}\left(\frac{\Delta x}{\Delta}\right)^2\right]$$

$$\tau_{13} = \tau_{31} = \rho_0 K_m S\left[\left(\frac{\partial u}{\partial z} + \frac{\partial w}{\partial x}\right)\left(\frac{\Delta z}{\Delta}\right)^2\right]$$

$$\tau_{23} = \tau_{32} = \rho_0 K_m S\left[\left(\frac{\partial v}{\partial z} + \frac{\partial w}{\partial y}\right)\left(\frac{\Delta z}{\Delta}\right)^2\right], \quad \text{(A7)}$$

where DIVM is defined by (A8) of LH88. This for-

mulation maintains the feature of having the trace τ_{kk} of the stress tensor vanish, but makes the vertical mixing terms independent of the horizontal grid intervals, in contrast to the form in LH88. In Eq. (A7) of LH88, the potential existed for an instability to develop in the τ_{13} and τ_{23} terms as Δx and Δy became larger, because of the $(\Delta x/\Delta)^2$ or $(\Delta y/\Delta)^2$ factor.

The factor S is now included in the vertical mixing of cloud- and rainwater, as discussed in LH88. This factor has the effect of reducing the vertical mixing of q_c and q_r in regions of stable stratification.

APPENDIX B

Lateral Boundary Condition for Normal Velocities

The Sommerfeld radiation condition is used for the normal velocity u_n

$$\frac{\partial u_n}{\partial t} = -c\frac{\partial u_n}{\partial x_n}, \tag{B1}$$

with c given by Eq. (2.1) of Orlanski (1976); namely,

$$c = \frac{\partial u_n/\partial t}{\partial u_n/\partial x_n} = \frac{u^{\tau}_{n\,\mathrm{IB}-1} - u^{\tau-2}_{n\,\mathrm{IB}-1}}{u^{\tau}_{n\,\mathrm{IB}-1} + u^{\tau-2}_{n\,\mathrm{IB}-1} - 2u^{\tau-1}_{n\,\mathrm{IB}-2}}\frac{\Delta x_n}{\Delta t}, \tag{B2}$$

where τ refers to the time level and IB is the boundary point. Thus, the value of $u^{\tau+1}_{n\,\mathrm{IB}}$ as given by Eq. (2.2) of Orlanski (1976) is

$$u^{\tau+1}_{n\,\mathrm{IB}} = \frac{[1-(\Delta tc/\Delta x_n)]}{[1+(\Delta tc/\Delta x_n)]}u^{\tau-1}_{n\,\mathrm{IB}} + \frac{2\Delta tc/\Delta x_n}{[1+(\Delta tc/\Delta x_n)]}u^{\tau}_{n\,\mathrm{IB}-1}. \tag{B3}$$

However, this expression cannot be used blindly without encountering some difficulties. An anelastic model with rigid upper and lower boundaries must have no net mass flux across its lateral boundaries in order to conserve mass. The Sommerfeld radiation condition does not automatically satisfy this condition, since the fluxes at the boundary points are independent of each other and do not have any integral constraint on their sum. For this reason, an adjustment is made to all the boundary mass-flux tendencies, proportional to their magnitudes, to assure a balance of inflow and outflow across the domain boundaries.

Problems also arise in the calculation of c by (B2). There is no guarantee that the value calculated will be $0 \leqslant c \leqslant \Delta x/\Delta t$, as is required in Orlanski's formulation. Both values of $c < 0$ and $c > \Delta x/\Delta t$ may be calculated. The standard fix for $c < 0$ is to set $c = 0$; for $c > \Delta x/\Delta t$ is to set $c = \Delta x/\Delta t$ (Orlanski 1976; Clark 1979). In this model, those limits have been modified to eliminate some problems present in the simulations.

One particular situation in which c is calculated to be negative by (B2) occurs when an extremum in u_n is located one grid point inside the boundary and is propagating outward. The standard fix of setting $c = 0$ gives $u^{\tau+1}_{n\mathrm{IB}} = u^{\tau-1}_{n\mathrm{IB}}$ from (B3), so that the value of u_n at the boundary is unchanged during the time step and the progress of the extremum is slowed. When the same flow is modeled on a larger domain, the extremum continues to propagate, indicating that the presence of the boundary has retarded its movement. To alleviate this spurious slowing under these conditions, c is set to $c = c^* + u_n$, rather than $c = 0$, where $c^* = 30$ m s^{-1}, typical of the faster gravity wave speeds in the model, and u_n is the model velocity on the lateral boundary, positive for outflow. An unpublished study by the first two authors indicates that this modification results in a closer balance between the inflow and outflow across the boundaries and a lessening of the adjustment necessary to conserve model mass.

Another problem that develops in this study with $\Delta x = 5$ km involves the upper limit on c. Having $c \leqslant \Delta x/\Delta t$ allows c to be as large as 500 m s^{-1}. This is much larger than any possible gravity-wave speed in the anelastic model. Therefore, the upper limit on c is changed to

$$c \leqslant c^* + u_n, \tag{B4}$$

where c^* and u_n are as defined above. Thus, for inflow velocities greater than or equal to 30 m s^{-1}, c is set to zero. Without this modification, excessively large values of c are calculated along some portions of the model perimeter, producing a large net mass flux across the boundaries. Mass conservation requirements then force compensatory tendencies elsewhere and result in convergence–divergence patterns near the boundaries. Implementation of this more realistic upper limit on c reduces the net mass flux and eliminates the spurious near-boundary convergence.

REFERENCES

Alberty, R. L., D. W. Burgess, C. E. Hane and J. F. Weaver, 1979: SESAME 1979 Operations Summary, NOAA/ERL, Boulder, 253 pp. [NTIS PC A13/MF A01.]

Anthes, R. A., Y.-H. Kuo, S. G. Benjamin and Y.-F. Li, 1982: The evolution of the mesoscale environment of severe local storms: Preliminary modeling results. *Mon. Wea. Rev.*, **110**, 1187–1213.

Bell, R. S., 1987: Evaluation of local weather forecasts produced by the Meteorological Office mesoscale model. *PSMP Reprint Series No. 25, Programme on Short- and Medium-Range Weather Prediction Research*, Geneva, World Meteor. Org., 149–152.

Blechman, J. B., 1981: Vortex generation in a numerical thunderstorm model. *Mon. Wea. Rev.*, **109**, 1061–1071.

Bluestein, H. B., and M. H. Jain, 1985: Formation of mesoscale lines of precipitation: Severe squall lines in Oklahoma during the spring. *J. Atmos. Sci.*, **42**, 1711–1732.

Chang, C. B., D. J. Perkey and C. W. Kreitzberg, 1981: A numerical case study of the squall line of 6 May 1975. *J. Atmos. Sci.*, **38**, 1601–1615.

Clark, T. L., 1979: Numerical simulations with a three-dimensional cloud model: Lateral boundary condition experiments and multicellular severe storm simulations. *J. Atmos. Sci.*, **36,** 2191–2215.

——, and R. D. Farley, 1984: Severe downslope windstorm calculations in two and three spatial dimensions using anelastic interactive grid nesting: A possible mechanism for gustiness. *J. Atmos. Sci.*, **41,** 329–350.

Kalb, M. W., 1985: Results from a limited area mesoscale numerical simulation for 10 April 1979. *Mon. Wea. Rev.*, **113,** 1644–1662.

Kessler, E., 1969: On the distribution and continuity of water substance in atmospheric circulations. *Meteor. Monogr.*, No. 32, Amer. Meteor. Soc., 84 pp.

Kirwan, A. D., 1969: Formulation of constitutive equations for large-scale turbulent mixing. *J. Geophys. Res.*, **74,** 6953–6959.

Klemp, J. B., and R. Rotunno, 1983: A study of the tornadic region within a supercell thunderstorm. *J. Atmos. Sci.*, **40,** 359–377.

——, and R. B. Wilhelmson, 1978: The simulation of three-dimensional convective storm dynamics. *J. Atmos. Sci.*, **35,** 1070–1096.

Kuo, Y.-H., and R. A. Anthes, 1984: Accuracy of diagnostic heat and moisture budgets using SESAME-79 field data as revealed by observing system simulation experiments. *Mon. Wea. Rev.*, **112,** 1465–1481.

Kurihara, Y., G. J. Tripoli and M. A. Bender, 1979: Design of a movable nested-mesh primitive equation model. *Mon. Wea. Rev.*, **107,** 239–249.

Lilly, D. K., 1962: On the numerical simulation of buoyant convection. *Tellus,* **14,** 148–172.

Lipps, F. B., and R. S. Hemler, 1982: A scale analysis of deep moist convection and some related numerical calculations. *J. Atmos. Sci.*, **39,** 2192–2210.

——, and ——, 1986: Numerical simulation of deep tropical convection associated with large-scale convergence. *J. Atmos. Sci.*, **43,** 1796–1816.

——, and ——, 1988: Numerical modeling of a line of towering cumulus on day 226 of GATE. *J. Atmos. Sci.*, **45,** 2428–2444.

Liu, J. Y., and H. D. Orville, 1969: Numerical modeling of precipitation and cloud shadow effects on mountain-induced cumuli. *J. Atmos. Sci.*, **26,** 1283–1298.

Moller, A., 1980: Mesoscale surface analysis of the 10 April 1979 tornadoes in Texas and Oklahoma. Preprints, *Eighth Conf. on Weather Forecasting and Analysis,* Denver, Amer. Meteor. Soc., 36–43.

Moore, J. T., and H. E. Fuelberg, 1981: A synoptic analysis of the first AVE-SESAME '79 period. *Bull. Amer. Meteor. Soc.*, **62,** 1577–1590.

National Climatic Center, 1979: Hourly Precipitation Data—Texas. Volume 29, Number 4, NOAA/EDIS, Asheville, 38 pp. [Available at National Climatic Center, Federal Building, Asheville, NC 28801.]

Orlanski, I., 1976: A simple boundary condition for unbounded hyperbolic flows. *J. Comput. Phys.*, **21,** 251–269.

Redelsberger, J. L., and J. P. Lafore, 1988: A three-dimensional simulation of a tropical squall line: Convective organization and thermodynamic vertical transport. *J. Atmos. Sci.*, **45,** 1334–1356.

Robert, A. J., 1966: The integration of a low order spectral form of the primitive meteorological equations. *J. Meteor. Soc. Japan,* **44,** 237–245.

Ross, B. B., 1987: The role of low-level convergence and latent heating in a simulation of observed squall line formation. *Mon. Wea. Rev.*, **115,** 2298–2321.

——, and I. Orlanski, 1982: The evolution of an observed cold front. Part I: Numerical simulation. *J. Atmos. Sci.*, **39,** 296–327.

Rotunno, R., J. B. Klemp and M. L. Weisman, 1988: A theory for strong, long-lived squall lines. *J. Atmos. Sci.*, **45,** 463–485.

Shapiro, R., 1972: Information loss and compensation in linear interpolation. *J. Comput. Phys.*, **10,** 65–84.

Vincent, D. G., and T. Q. Carney, 1982: Meso-synoptic scale circulation patterns during severe weather outbreaks of 10–11 April 1979. Preprints, *12th Conf. on Severe Local Storms,* San Antonio, Amer. Meteor. Soc., 556–559.

——, ——, J. H. Homan and R. Fulton, 1981: Mesoscale weather patterns during 10–11 April 1979 severe weather outbreak in the southwestern USA. *Proc. from the Joint IAMAP/IAGA Symp.,* Hamburg, European Space Agency, 11–16.

Weisman, M. L., and J. B. Klemp, 1982: The dependence of numerically simulated convective storms on wind shear and buoyancy. *Mon. Wea. Rev.*, **110,** 504–520.

——, —— and R. Rotunno, 1988: Structure and evolution of numerically simulated squall lines. *J. Atmos. Sci.*, **45,** 1990–2013.

Wilhelmson, R. B., and C.-S. Chen, 1982: A simulation of the development of successive cells along a cold outflow boundary. *J. Atmos. Sci.*, **39,** 1466–1483.

Williams, G. P., 1972: Friction term formulation and convective instability in a shallow atmosphere. *J. Atmos. Sci.*, **29,** 870–876.

Zack, J. W., V. C. Wong, M. L. Kaplan and G. D. Coats, 1983: A nested grid mesoscale numerical simulation of an isolated tornadic convective complex. Preprints, *13th Conf. on Severe Local Storms,* Tulsa, Amer. Meteor. Soc., 336–341.

Zhang, D.-L., and J. M. Fritsch, 1986: Numerical simulation of the meso-β-scale structure and evolution of the 1977 Johnstown flood. Part I: Model description and verification. *J. Atmos. Sci.*, **43,** 1913–1943.